

3 **Cosmicflows-4**

4 R. BRENT TULLY,¹ EHSAN KOURKCHI,¹ HÉLÈNE M. COURTOIS,² GAGANDEEP S. ANAND,³ JOHN P. BLAKESLEE,⁴
5 DILLON BROUT,⁵ THOMAS DE JAEGER,¹ ALEXANDRA DUPUY,⁶ DANIEL GUINET,² CULLAN HOWLETT,⁷ JOSEPH B. JENSEN,⁸
6 DANIEL POMARÈDE,⁹ LUCA RIZZI,¹⁰ DAVID RUBIN,¹¹ KHALED SAID,⁷ DANIEL SCOLNIC,¹² AND BENJAMIN E. STAHL¹³

7 ¹*Institute for Astronomy, University of Hawaii, 2680 Woodlawn Drive, Honolulu, HI 96822, USA*

8 ²*University of Lyon, UCB Lyon 1, CNRS/IN2P3, IUF, IP2I Lyon, France*

9 ³*Space Telescope Science Institute, 3700 San Martin Drive, Baltimore, MD 21218, USA*

10 ⁴*Gemini Observatory & NSF's NOIRLab, 950 N. Cherry Ave., Tucson, AZ 85719, USA*

11 ⁵*Center for Astrophysics, Harvard & Smithsonian, 60 Garden St., Cambridge, MA 02138, USA*

12 ⁶*Korea Institute for Advanced Study, 85, Hoegi-ro, Dongdaemun-gu, Seoul 02455, Republic of Korea*

13 ⁷*School of Mathematics and Physics, The University of Queensland, Brisbane, QLD 4072, Australia.*

14 ⁸*Department of Physics, Utah Valley University, 800 W. University Parkway, Orem, UT 84058, USA*

15 ⁹*Institut de Recherche sur les Lois Fondamentales de l'Univers, CEA Université Paris-Saclay, 91191 Gif-sur-Yvette, France*

16 ¹⁰*W.M. Keck Observatory, 65-1120 Mamalahoa Highway, Kamuela, HI 96743, USA*

17 ¹¹*Department of Physics & Astronomy, University of Hawaii at Manoa, Honolulu, HI 96822, USA*

18 ¹²*Department of Physics, Duke University, Durham, NC 27708, USA*

19 ¹³*Department of Astronomy, University of California, CA 94720-3411, USA*

20 **ABSTRACT**

21 With *Cosmicflows-4*, distances are compiled for 55,877 galaxies gathered into 38,065 groups. Eight
22 methodologies are employed, with the largest numbers coming from the correlations between the pho-
23 tometric and kinematic properties of spiral galaxies (TF) and elliptical galaxies (FP). Supernovae that
24 arise from degenerate progenitors (SNIa) are an important overlapping component. Smaller contrib-
25 utions come from distance estimates from the surface brightness fluctuations of elliptical galaxies
26 (SBF) and the luminosities and expansion rates of core collapse supernovae (SNII). Cepheid Period-
27 Luminosity Relation (CPLR) and Tip of the Red Giant Branch (TRGB) observations founded on
28 local stellar parallax measurements along with the geometric maser distance to NGC 4258 provide the
29 absolute scaling of distances. The assembly of galaxies into groups is an important feature of the
30 study in facilitating overlaps between methodologies. Merging between multiple contributions within
31 a methodology and between methodologies is carried out with Bayesian Markov chain Monte Carlo
32 procedures. The final assembly of distances is compatible with a value of the Hubble constant of
33 $H_0 = 75.0 \text{ km s}^{-1} \text{ Mpc}^{-1}$ with the small statistical error $\pm 0.8 \text{ km s}^{-1} \text{ Mpc}^{-1}$ but a large potential
34 systematic error $\sim 3 \text{ km s}^{-1} \text{ Mpc}^{-1}$. Peculiar velocities can be inferred from the measured distances.
35 The interpretation of the field of peculiar velocities is complex because of large errors on individual
36 components and invites analyses beyond the scope of this study.

37 **1. INTRODUCTION**

38 *Cosmicflows* is a program to compile galaxy distances
39 and parse observed velocities into components due to
40 the expansion of the universe and residuals due to grav-
41 itational interactions. The fundamental interest is to
42 derive inferences regarding the large scale structure of
43 the universe from galaxy test particle peculiar motions.
44 This fourth release of the program follows those of Tully
45 et al. (2008, 2013, 2016).

46 Contributions to the *Cosmicflows* program have come
47 from work within our collaboration and from the litera-
48 ture. We consider methodologies that have been tested
49 and have physical bases that are reasonably well under-
50 stood. It is as great a consideration, though, that there

51 be large overlaps between contributions. A sample with
52 distances to only a few objects cannot confidently be
53 meshed within a common scale so is not very useful.

54 We derive distances in significant numbers mainly
55 from seven methodologies. By far, the largest quantita-
56 tive contributions are given by the Fundamental Plane
57 (FP) correlation between the luminosity, surface bright-
58 ness, and central velocity dispersion of early-type galax-
59 ies (Dressler et al. 1987b; Djorgovski & Davis 1987) and
60 the luminosity-rotation rate relation for spiral galaxies
61 (Tully & Fisher 1977) (TFR or TF). The individual er-
62 rors in these cases are substantial (20–25%) but the ob-
63 jects are widely dispersed, providing a dense network of
64 distance information across the sky extending to $\sim 0.05c$

and in the celestial and galactic north to $z = 0.1$, the upper cutoff of our compilation.

Three other methods probe substantial distances with greater accuracy but their contributions remain small. Supernovae of type Ia (SNIa) (Phillips 1993) provide distances with accuracy $\sim 7\%$ out to $0.1c$. Supernovae of type-II (SNII) (Hamuy & Pinto 2002) provide distances with $\sim 15\%$ accuracy to similar distances. Surface brightness fluctuations (SBF) monitoring the degree of resolution of the old stellar populations of elliptical galaxies (Tonry & Schneider 1988) can give distances with $\sim 5\%$ accuracy to targets within $\sim 0.03c$.

While comparisons between these five methods can be set on a common relative scale, it remains to give them an absolute calibration. Two methods provide a bridge: those provided by the Cepheid period-luminosity relation (CPLR) (Leavitt & Pickering 1912) and the constancy of stellar luminosities at the tip of the red giant branch (TRGB) (Lee et al. 1993). These methods provide accurate distances ($\sim 5\%$) but are restricted to less than ~ 20 Mpc.

There has been considerable effort to establish the absolute scale of the CPLR and TRGB procedures through geometrically based observations. Parallax distances can be established to Cepheids within our own galaxy (Benedict et al. 2007) and parallax distances to RR Lyrae and horizontal branch stars can establish the TRGB scale (Rizzi et al. 2007). It is anticipated that observations with GAIA (Clementini et al. 2018; Mould et al. 2019) will provide robust direct Cepheid and TRGB calibrations in the near future. Meanwhile, important links to an absolute scale are provided by detached eclipsing binaries in the Large Magellanic Cloud (Pietrzyński et al. 2019) and the maser system in the nuclear region of the galaxy NGC 4258 (Reid et al. 2019).

The main contributions in the first edition of *Cosmicflows* (Tully et al. 2008) were based on the TFR with optical photometry obtained object by object and analog neutral Hydrogen ($\text{H}\alpha$) linewidths. The catalog contained distances to 1,791 galaxies constrained to the limit $3,000 \text{ km s}^{-1}$.

Cosmicflows-2 (Tully et al. 2013) was expanded to include a much larger volume, peaking in numbers at $5,000 \text{ km s}^{-1}$ with a tail extending to $\sim 15,000 \text{ km s}^{-1}$. Most of the contributions came from the TFR, with as a major revision the employ of a rigorous algorithm in the reduction of digital $\text{H}\alpha$ spectra (Courtois et al. 2009, 2011b). Likewise, the photometric analysis was more rigorously defined (Courtois et al. 2011a; Sorce et al. 2012). The catalog then grew to include 8,188 galaxies.

The major addition to *Cosmicflows-3* (Tully et al. 2016) were FP distance measures from the 6dFGSv sur-

vey (Springob et al. 2014). This sample is entirely confined to the celestial south and abruptly cuts off at $16,000 \text{ km s}^{-1}$. A secondary addition came from the TFR method with infrared photometry provided by the Spitzer Space Telescope (Sorce et al. 2014). *Cosmicflows-3* provided distances for 17,699 galaxies. Coverage within $\sim 8,000 \text{ km s}^{-1}$ was reasonably balanced around the sky but at $8,000$ to $16,000 \text{ km s}^{-1}$ it strongly favored the southern hemisphere. The infrared TFR contribution was confined to within $\sim 6,000 \text{ km s}^{-1}$ but notably extended coverage to low galactic latitudes, shrinking the coverage gap between galactic hemispheres.

Here with *Cosmicflows-4* a most important addition is a much extended TFR sample of 10,000 galaxies drawing in particular on kinematic information from ALFALFA, the Arecibo Legacy Fast ALFA survey of the high galactic latitude sky in the declination range $0 - 38$ degrees (Haynes et al. 2011, 2018). Photometry is provided by SDSS, the Sloan Digital Sky Survey (York et al. 2000) and WISE, the Wide-field Infrared Explorer (Wright et al. 2010). This component of *Cosmicflows-4* substantially redresses the imbalance favoring the southern sky of the previous catalog.

SDSS also provides the source material for a second even larger addition to the current catalog. SDSS photometry and spectroscopy are combined to provide FP distances to 34,000 galaxies out to $30,000 \text{ km s}^{-1}$ in the quadrant of the sky that is celestial north and galactic north. In consequence, while *Cosmicflows-3* tilted toward coverage of the celestial south, now *Cosmicflows-4* greatly expands our knowledge of the north.

With the astronomical community's overriding interest in precision distance measurements in order to secure the value of the Hubble constant, there are understandable arguments for a maximally homogeneous approach (Riess et al. 2016). The *Cosmicflows* assembly is heterogeneous. It is to be appreciated that the primary interest of this program is the mapping of *deviations* from cosmic expansion, requiring coherence of distance measurements but not an absolute scaling. Nonetheless, the reasonable establishment of a zero point is not our most difficult task. Our heterogeneous approach has virtues. Results from separate methodologies can be compared by sectors of the sky or distance, potentially revealing systematics. Different contributions favor ancient populations or young, members of clusters or the field. Some are better probes of low galactic latitudes. Our samples are heterogeneous but not indiscriminate.

Coincidences of distance measurements by different methodologies to members of a common group enables the stitching of samples into a coherent ensemble. Our

discussion will turn first to the important matter of the definition of groups in §2. Subsequent sections will give attention to each of the seven methodologies that provide most of our distances. We begin with the numerically dominant TFR (§3) and FP (§4) components, benefiting from overlaps between large samples to establish coherence in a core compilation. We then give attention to the SBF (§5) and SNIa (§6) contributions that are modest in number but that impose demanding constraints. There is a brief discussion of SNII (§6.2) that at this point makes a relatively small contribution. This entire edifice is then be linked to foundational TRGB (§7) and CPLR (§8) information, these in turn grounded by geometrical maser¹, eclipsing binary, and parallax observations. The integration of methodologies is discussed in §10. The data products and a brief description of properties are given attention in §12 and §13. Then §14 provides a summary.

2. GALAXY GROUPS

Galaxies tend to lie in groups, large and small. If associations are made correctly, then all distance measures to galaxies in a group should be the same within uncertainties. The composition of galaxy groups, then, is of major importance for our study for at least three reasons. First, averaging over the properties of a group reduces errors. With weighted averaging of distances, uncertainties can be brought down from single case 20–25% values (depending on the methodology) to statistical uncertainties of a few percent with some rich clusters. The gains apply to velocities as well. Velocity averaging can encompass *all* known group members, not just those with measured distances. Second, it is particularly important in the modeling of galaxy flows to accurately locate the rich clusters, where distance measures from at least the fundamental plane and surface brightness fluctuation targets congregate. Rich clusters tend to lie at focal points of galaxy streams.

Third, and perhaps most important, it is through the groups that we most effectively match the zero point scaling of the diverse samples. Given the potential for systematics within samples, across sectors of the sky, and with distance, the more overlap the better. While there can be some overlap at the level of individual galaxies, by far most of our overlaps occur at the level of groups and clusters. A corollary benefit is the ability, in comparing distances to objects in common, to weed out egregiously bad data.

¹ Studies of nuclear maser systems provide an eighth methodology and one that gives independent absolute distance estimates but these are only available for six galaxies. Discussed in §9.

Galaxy groups come in a wide range of scales. We want to benefit from the advantages of grouping over the full range down to the instances of pairs. Typical friends-of-friends and related group algorithms do not scale physically over the three decades of mass of interest ($10^{12} - 10^{15} M_{\odot}$). Appreciating the importance of the matter, we initiated studies resulting in three papers. In the first (Tully 2015a), we gave detailed attention to eight well-studied groups/clusters ranging from the Local Group to the Coma Cluster. It was possible in these eight clean cases to isolate an observable proxy for the virial radius of collapsed halos; the radius of second turnaround, R_{2t} (related to the "splashback" radius (Adhikari et al. 2014)). This radius is found to scale, as theory predicts, as $R_{2t} \propto M^{1/3}$ and $R_{2t} \propto \sigma_p$ for halos (groups, clusters) with mass M and velocity dispersion σ_p . This first paper establishes the coefficients of the scaling relationships.

In the second paper (Tully 2015b), the scaling relationships were applied to build a group catalog involving 43,000 galaxies in the 2MASS redshift survey essentially complete over the sky at $|b| > 5^{\circ}$ for galaxies brighter than $K_s = 11.75$ (Huchra et al. 2012). The 2MASS survey, given its sensitivity to old stars, gives good representation of the mass distribution within the volume extending to $15,000 \text{ km s}^{-1}$ that is our principal concern. Relative distances are based on redshifts. We favor the use of this group catalog at systemic velocities greater than $\sim 3000 \text{ km s}^{-1}$. Were we to consider an alternative we would use the similarly physically motivated catalog by Lim et al. (2017).

Nearer than $\sim 3000 \text{ km s}^{-1}$ confusion arising from peculiar velocities is severe and we have knowledge of a profusion of low surface brightness galaxies that fail to enter the 2MASS catalog. Hence, for the nearby volume we turn to the group catalog assembled in the third paper (Kourkchi & Tully 2017), based on a heterogeneous collection of all 15,000 galaxies with known velocities within $3,500 \text{ km s}^{-1}$. The groups are constituted based on the same scaling relations. The availability of distance information from *Cosmicflows-3* is tremendously helpful in resolving confusion issues and evaluating masses, hence scaling parameters.

With both the near and far catalogs, the groups are roughly bounded by the radius of second turnaround. Hence they represent collapsed halos. As a naming convention, we identify a group by the Principal Galaxies Catalog number (Paturel et al. 1996) of the dominant member, which we call 1PGC. There can be inconsistencies between the two catalogs within $3,500 \text{ km s}^{-1}$. In such cases we favor the specifications by Kourkchi & Tully (2017).

These group catalogs provide an excellent description of clustering within $\sim 15,000 \text{ km s}^{-1}$, the useful range of the 2MASS $K_s = 11.75$ redshift survey. However the SDSS based FP sample extends to $0.1c$. This SDSS FP sample is a sub-component of the Tempel et al. (2014, 2017) SDSS group catalogs. The supernova samples also extend to $z = 0.1$, well beyond the range of the Tully (2015b) groups. If a group affiliation is unavailable for a galaxy within the groups described above then we opt for memberships in the 2017 Tempel et al. catalog. The relevant galaxies have PGC identifications. We take as the 1PGC name for a Tempel et al. group the PGC number of the brightest member within our catalog.

3. LUMINOSITY-LINEWIDTH DISTANCES TO SPIRAL GALAXIES

Distances derived from the TFR are an extremely important component of the *Cosmicflows* program. They are numerous and the most widely distributed. Spiral galaxies are found in all environments, providing links with other methodologies in groups and sparse but invaluable coverage in voids.

3.1. The Baryonic TFR

Conventionally in the past, TFR samples have been acquired by individual targeting of selected candidates for both the photometric (imaging) and kinematic (linewidth) required components. Nowadays, wide field optical, infrared, and H I radio surveys give access to much larger samples. Specifically, here, we make use of serendipitous Sloan Digital Sky Survey (SDSS) DR12 u, g, r, i, z optical imaging (Alam et al. 2015), Wide-field Infrared Satellite Explorer (WISE) $W1$ and $W2$ infrared imaging (Wright et al. 2010; Mainzer et al. 2011), and Arecibo Legacy Fast ALFA Survey (ALFALFA) neutral Hydrogen spectral detections (Haynes et al. 2018), supplemented in the radio with pointed observations with the Green Bank Telescope and Parkes Telescope (Dupuy et al. 2021).

In a suite of three papers, we explored properties of the optical and infrared photometric material particularly pertaining to issues of extinction (Kourkchi et al. 2019), then gave optical and infrared calibrations of the TFR based on ~ 600 galaxies in 20 clusters (Kourkchi et al. 2020a), and then used the calibrations to derived TFR distances for $\sim 10,000$ galaxies (Kourkchi et al. 2020b). It was subsequently revealed that the distances in the latter publication are affected by a bias: a trend in Hubble parameter values, $H_i = fc_z/d_i$, as functions

of apparent magnitude.² The bias strongly affects distance estimates to intrinsically fainter galaxies within $4,000 \text{ km s}^{-1}$ and arises from faint end curvature in the TFR. Distances to galaxies with velocities greater than $4,000 \text{ km s}^{-1}$ are mildly affected.

Much, and even a majority, of baryonic mass in faint galaxies is in the form of interstellar gas. It has been noted that adding this constituent to the stellar component represented by optical or infrared light, formulating the baryonic Tully-Fisher relation (BTFR), effectively linearizes the relation between the logarithms of baryonic mass and H I profile linewidth (McGaugh et al. 2000; McGaugh 2005; Lelli et al. 2016, 2019). Consequently, and in response to our concern regarding the bias with faint galaxies in the TFR study by Kourkchi et al. (2020b), the same sample has been re-analyzed with the BTFR methodology by Kourkchi et al. (2022).

The BTFR requires the additional component of H I fluxes, an observable acquired simultaneously with linewidths. The need for a robust H I detection gives focus to the condition that the sample is H I flux limited: photometry for any target with sufficient H I flux is easily obtained. However, an H I flux limit translates to a cut in gas mass that increases with distance. This trend results in a bias that must be addressed in order to obtain distance measures of value. Kourkchi et al. (2022) developed a procedure that was demonstrated with mock data to provide unbiased distance estimates.

Application of the BTFR also requires the translation of luminosities into approximations of stellar mass, involving color terms. The conversions are linear, but uncertainties are further compounded by the summation of stellar and gas mass components. On the one hand, there is a greater complexity with the BTFR but on the other hand the linkage with the dark matter dominated total mass is expected to be tighter. Scatter as evaluated from H_i values at $V > 4,000 \text{ km s}^{-1}$ is 22% in distances, comparable to that with the TFR. Kourkchi et al. (2022) provide BTFR distance estimates for 9967 galaxies.

3.2. Ensemble of TFR and BTFR Sources

Cosmicflows-4 assembles TFR distances to 12,412 galaxies, the largest, most coherent compilation to date by this methodology. The most important contribution (9,967 galaxies) is the new BTFR sample discussed by Kourkchi et al. (2022) (hereafter “cf4”). This new sample is compared and merged with five TFR samples: the assembly of 5,980 cases in *Cosmicflows-2* that itself is

² The cosmological model parameter f is defined in connection with Eq. 3.

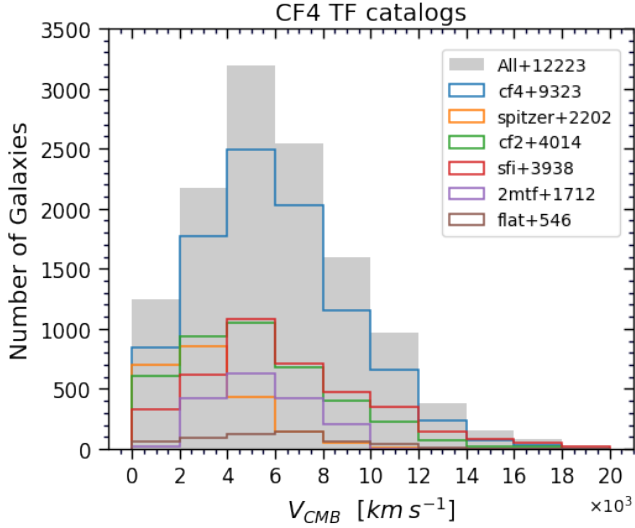


Figure 1. Cumulative histogram of TF targets with systemic velocity and a breakdown by sub-sample as given by the legend.

broken into a part (4,069) derived within our collaboration (hereafter “cf2”) and a part (3,957) emanating from the SFI++ study (Springob et al. 2007) (hereafter “sfi”), 2,251 galaxies discussed in *Cosmicflows-3* incorporating photometry from Spitzer Space Telescope images (“spitzer”), 1,715 galaxies utilizing 2MASS photometry (“2mtf”) (Hong et al. 2019), and 551 extreme edge on galaxies (Makarov et al. 2018) (“flat”).

Figure 1 is a histogram of the run of velocities for the TF sub-samples and the full TF sample. The distribution of the combined TF sample is displayed in supergalactic coordinates in Figure 2. The bands of high object density crossing the two supergalactic hemispheres lie in the $0 < \delta < 38$ declination zone accessed by Arecibo Telescope.

Our analysis began with each sample alone. At systemic velocities above 4,000 km s $^{-1}$ cosmic expansion velocities are expected to overwhelmingly dominate deviant velocities. Hence, a necessary (not sufficient) criterion a sample should satisfy is approximate constancy in the Hubble parameter for individual galaxies, f_{cz_i}/d_i , averaged in velocity bins. The results of this test for all but the most recent flat galaxy sample were presented in Kourkchi et al. (2020b). A significant drift toward smaller $\langle H_i \rangle$ (larger derived distances) was evident in the “2mtf” sample. An adjustment to negate this trend was introduced by Kourkchi et al. (2020b), see §5, and is incorporated in the current work. The “flat” sample passes the $\langle H_i \rangle$ constancy test. Note that absolute $\langle H_i \rangle$ values are not an issue at this stage; they can be (and are) different for each sample.

This test of the constancy of H_i with redshift provides as a side product an evaluation of the *rms* dispersion in measurements within each sample. The measured values include dispersion in velocities and intrinsic dispersion but these components are unimportant if, as we do, we restrict attention to velocities greater than 4,000 km s $^{-1}$. We find the following characteristic *rms* dispersions for seven samples (treating separately the optical and infrared components of “cf4” (whence, “cf4-op” and “cf4-ir”), the two components of *Cosmicflows-2*, “cf2” and “sfi”, and the components of “spitzer” with and without color corrections (“spitzer-cc” and “spitzer-nc”). The *rms* dispersions for the BTFR “cf4-ir” and “cf4-op” are 0.45 and 0.47 mag respectively, while for the two-parameter TF studies dispersions are 0.40 for all three “cf2”, “sfi”, and “spitzer-cc”, 0.50 for both “spitzer-nc” and “2mtf”, and 0.55 for “flat”. Distance values for “2mtf” at local group frame velocities less than 2000 km s $^{-1}$, as evaluated by the Hubble parameter test and the test to be discussed next, are systematically too low and we reject all those “2mtf” measurements.

Another test of the samples applied by Kourkchi et al. (2020b) was to give attention to differences in distance moduli between “cf4” and an alternate sample: $\langle \mu_{cf4} - \mu_{alt} \rangle$ where alt is any of the other samples (now extended to include “flat”). This test is particularly useful for the isolation of egregiously bad distance values in one of the samples. Well less than 1% of cases in “cf2”, “sfi”, “spitzer”, and “cf4” are rejected by this test. With “2mtf” $\sim 2\%$, and with “flat” $\sim 5\%$, are rejected.

We now give attention to the integration of these samples into a global maximally consistent compilation of TFR distances.

3.3. Preliminaries

Our goal is to combine the distinct TFR sub-samples into a single TFR sample. Before this integration, each sub-sample has its own zero point scaling. Here we revise the zero points of sub-samples to achieve statistical equality between them. We stress that we do not make relative changes in moduli *within* a sub-sample in this process. Doing so would subvert the utility provided by multiple sub-samples in reducing systematics.

It is evident that TFR samples have non-Gaussian outliers. Steps have been described to remove strongly deviant cases but our initial integration of sub-samples reveals additional instances. Applying a 3.5σ rejection criterion caught 275 cases among 22,233 measures (1.2%) where there would be 9 with a normal distribution. These outliers are removed.

Next, we want to profit from the advantages of averaging over groups discussed in §2. We begin by weighted

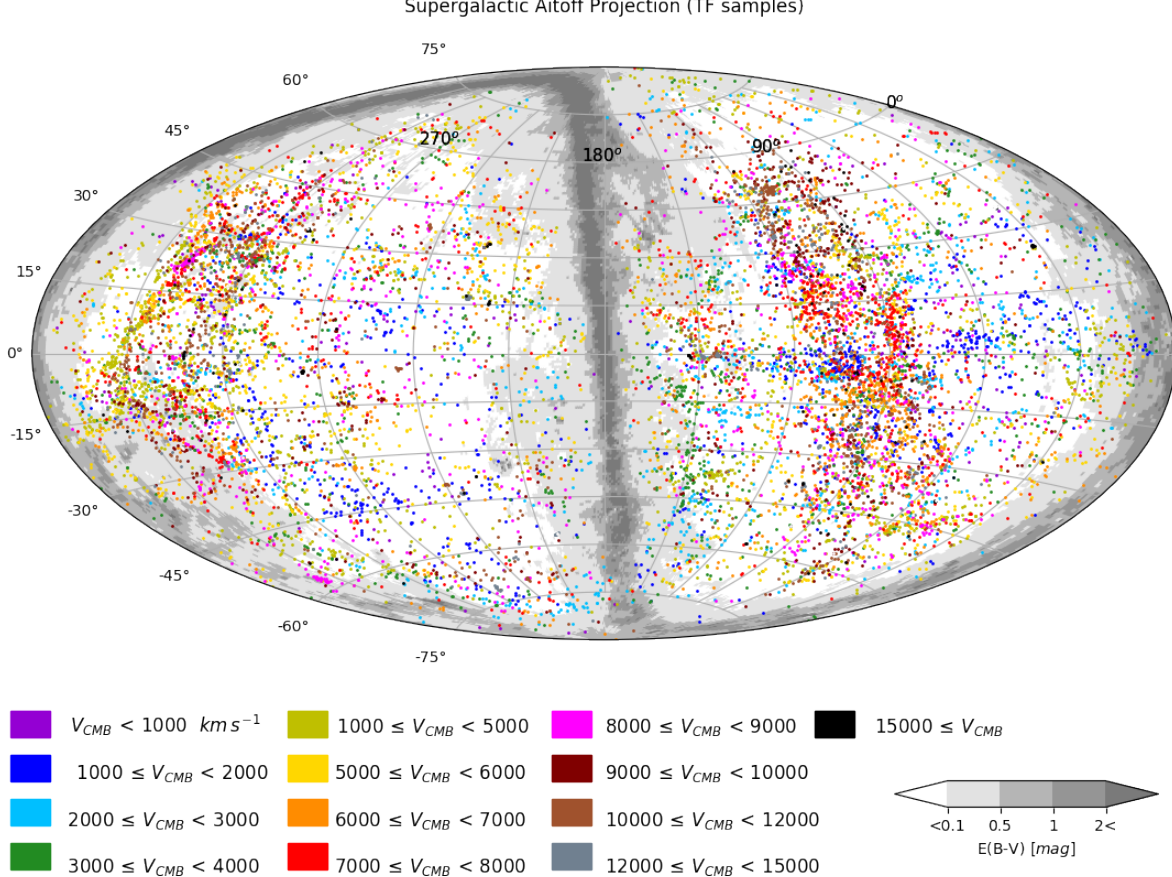


Figure 2. An Aitoff projection in supergalactic coordinates of the distribution of the 12223 galaxies constituting ensemble of TFR samples. Colors relate to systemic velocities of the group of a galaxy as given in the table below the map. Milky Way extinction levels are cast in shades of gray. The dense roughly vertical swaths of objects in both supergalactic hemispheres lie in the declination band of the Arecibo Telescope.

averaging of the distance moduli of all galaxies within a 1PGC group within a single sub-sample. Individual weights are formed from the inverse square of rms uncertainties. This average and associated weight is one object in the ensuing analysis. Accordingly, each sub-sample is reduced to a quantity of objects (halos, groups, clusters) composed of from one to many individual galaxies, each identified by a 1PGC number.

3.4. Combining all TFR distances: Bayesian approach

Ultimately, we want to merge all samples by all methodologies into a coherent set with a zero point established by geometric distance measurements. At this stage, it is sufficient to bring all TFR sub-samples onto a common scale. The baseline TFR scale will be set by our new “cf4” sub-sample that should lie close to our final scale, given its linkage to Cepheid and TRGB measures as discussed by Kourkchi et al. (2020a,b, 2022).

Here, we pursue our goal to find the global modulus offset of each sample, “s”, from that of “cf4”, where

“s” stands for any of the samples we introduced earlier in this chapter (“cf2”, “sfi”, “spitzer”, “2mtf”, “flat”). We will adjust the reported distance moduli within each sample, $DM_{in}^{(s)}$, following $DM^{(s)} = DM_{in}^{(s)} + \Delta\mu_s$ in order to set all cataloged distances on the same scale. By our convention, $\Delta\mu_{cf4} = 0$. We treat these adjusting values as a set of free parameters that are optimized together in a Bayesian framework. The best offset parameters minimize the total deviation of adjusted object distance moduli (groups and individual galaxies) from the weighted distance modulus averages offered by all samples together.

Our objective is to find the posterior probability distribution $\mathcal{P}(\Theta|\mathcal{D})$, with Θ being the vector of all moduli offsets, $(\Delta\mu_{s1}, \Delta\mu_{s2}, \dots)$. \mathcal{D} holds the original catalogued distance moduli, $DM_{in}^{(s)}$. According to conditional probability theory, $\mathcal{P}(\Theta|\mathcal{D}) \propto \mathcal{P}(\mathcal{D}|\Theta)\mathcal{P}(\Theta)$. Having no prior knowledge about the distribution of the moduli offsets implies $\mathcal{P}(\Theta) = 1$ and subsequently $\mathcal{P}(\Theta|\mathcal{D}) \propto \mathcal{P}(\mathcal{D}|\Theta)$, where the right hand side is the likelihood function, \mathcal{L} .

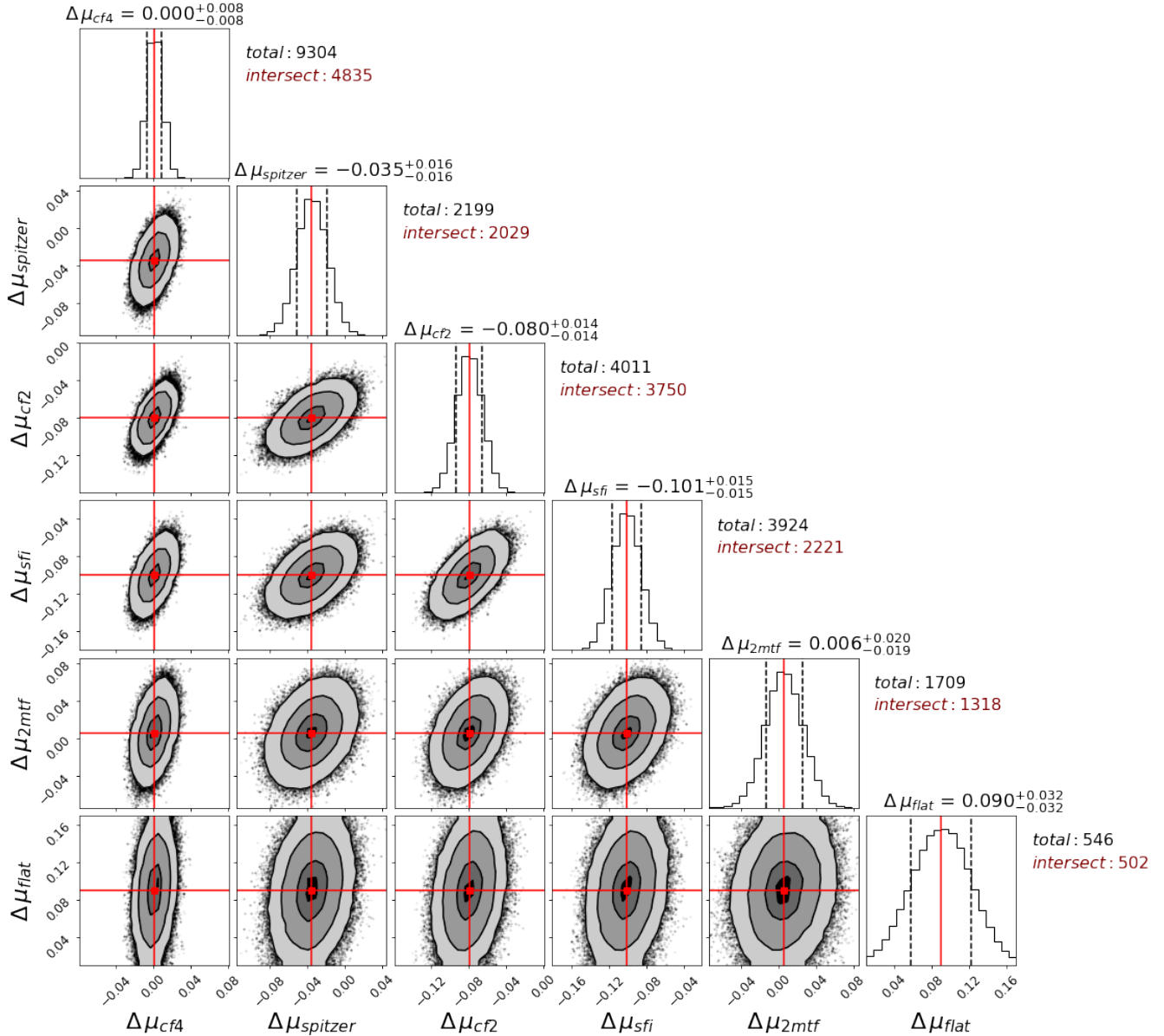


Figure 3. The posterior distribution of the optimized zero points of TFR catalogs with respect to “cf4”. Contours represent $\sigma/2$, σ , $3\sigma/2$ and 2σ levels of the 2-dimensional distributions and they enclose 12%, 39%, 68% and 86% of the distributed points respectively. Two vertical dashed lines in each of the 1-dimensional histograms specify the region that accommodates 68% of the points, and the red vertical line identifies the median of the distribution. Each panel covers ± 0.08 mag about the center of distribution.

We assume that all measured object distances are independent with Gaussian uncertainties. Therefore, for each object, n , the likelihood function is the multiplication of a set of independent probabilities given as

$$\mathcal{L}_n = \prod_{All ``s"} \frac{1}{\sqrt{2\pi\sigma_{n,s}^2}} \exp \frac{-1}{2} \left(\frac{DM_n^{(s)} - \langle DM \rangle_n}{\sigma_{n,s}} \right)^2, \quad (1)$$

iterating over all distance catalogs. $\langle DM \rangle_n$ is the weighted average distance modulus of the n^{th} object

that is derived from the adjusted distance moduli, $DM_n^{(s)}$ is the distance modulus of the object in the sample “s”, and $\sigma_{n,s}^2$ is the variance of $DM_n^{(s)} - \langle DM \rangle_n$, that is determined by adding the uncertainties of the associated parameters in quadrature. Likewise, the total likelihood function for all objects is $\mathcal{L}_{tot} = \prod_{n=1}^N \mathcal{L}_n$, where N is the total number of objects (groups and individuals). It is simpler to work with the logarithm of the likelihood function which is expressed as $\log \mathcal{L}_{tot} =$

499 $-\sum_{n=1}^N \chi_n^2 / 2$, where

$$\chi_n^2 = \left(\frac{DM_n^{(s)} - \langle DM \rangle_n}{\sigma_{n,s}} \right)^2. \quad (2)$$

500 Adopting a flat prior distribution for the moduli off-
 501 sets leaves us with a χ^2 minimization problem. We
 502 are interested in a set of moduli offsets that minimizes
 503 $\chi_{tot}^2 = \sum_{n=1}^N \chi_n^2$.

504 To sample the posterior distribution, $\mathcal{P}(\Theta|\mathcal{D})$, we
 505 use the Python package *emcee* (Foreman-Mackey et al.
 506 2013), that implements Markov Chain Monte Carlo
 507 (MCMC) simulations to explore the parameter space.
 508 Starting from our likelihood function, we generate 128
 509 chains each with the length of 10,000. We remove the
 510 first 1,000 steps which is conservatively chosen to en-
 511 sure that the remaining steps adhere to Markov chain
 512 statistics. Figure 3 illustrates the corner plots for the
 513 resulting posterior distribution of $\Delta\mu_s$. The top-most
 514 panel of each column shows the one dimensional distri-
 515 bution of the corresponding sampled parameter, over-
 516 laid with the median values (red solid line) and the
 517 lower/upper bounds corresponding to 16/84 percentiles
 518 (black dashed line). Horizontal and vertical red lines
 519 in the 2-dimensional distributions exhibit the location
 520 of the median values that are adopted as the optimum
 521 moduli offsets of the corresponding catalogs with respect
 522 to “cf4”.

523 The variance for a given sub-sample that is recorded
 524 in Fig. 3 depends on both the uncertainties in indi-
 525 vidual measurements and the number of intersections
 526 with other sub-samples. The individual uncertainties
 527 between the alternate TF sub-samples are only mod-
 528 estly different, so it is the numbers of intersections that
 529 dominate.

530 4. FUNDAMENTAL PLANE DISTANCES TO 531 EARLY-TYPE GALAXIES

532 The Fundamental Plane (FP) methodology (Dressler
 533 et al. 1987b; Djorgovski & Davis 1987), with its applica-
 534 bility to early-type galaxies, provides a complement to
 535 the TFR. The accuracies of individual measurements are
 536 comparable. While the gas-rich systems observed with
 537 the TFR are widely dispersed, the old star dominated
 538 systems favored for FP observations tend to clump in
 539 regions of high density.

540 Here in *Cosmicflows-4* we combine results from five
 541 programs. Three of these were already included in
 542 *Cosmicflows-2*: contributions for a total of 1508 galax-
 543 ies to be referred to as “smac” (Hudson et al. 2001),
 544 “efar” (Colless et al. 2001), and “enear” (Bernardi et al.
 545 2002). Individually these sources provide distances for
 690, 696, and 447 galaxies, respectively. Contributions

547 from a fourth program, 6dFGSv (Springob et al. 2014)
 548 were included in *Cosmicflows-3*. This sample of 7,099
 549 galaxy distances is particularly important as the numeri-
 550 cally dominant source of distances in the celestial south.
 551 However, by far the largest sample containing 34,059
 552 galaxies is a new contribution restricted to the celestial
 553 and galactic north that draws on data extracted from
 554 the Sloan Digital Sky Survey (SDSS). The three earliest
 555 FP surveys, “smac”, “efar”, and “enear” provide valua-
 556 ble bridges across the celestial hemispheres, important
 557 given there is only slight overlap (41 cases) between the
 558 6dFGSv and SDSS samples.

559 4.1. The 6dFGSv Sample

560 While the 6dFGSv sample was originally included in
 561 *Cosmicflows-3*, in this latest work we provide a new re-
 562 calibration of this sample based on the findings of Qin
 563 et al. (2018) designed to explore and remove spurious
 564 flows. In total, the 6dFGSv sample subtends the en-
 565 tire $\delta < 0^\circ$ sky, except for regions with galactic lati-
 566 tude $|b| < 10^\circ$. Its 8,885 objects incorporate many of
 567 the brightest early-type galaxies in the 6-degree Field
 568 Galaxy Survey (6dFGS; Jones et al. 2009), nominally
 569 selected to have a spectral SNR > 5 , total J -band mag-
 570 nitude < 13.65 , redshift $cz < 16,500 \text{ km s}^{-1}$ and veloci-
 571 ty dispersion greater than 112 km s^{-1} (Campbell et al.
 572 2014). Further refinements to this selection include vi-
 573 sual classification and removal of galaxies based on their
 574 morphological type (although as demonstrated in Tully
 575 et al. (2016) not all remaining galaxies are classified as
 576 ellipticals) and removal of objects with undesirable spec-
 577 tral features or poor spectral template fits (Campbell
 578 et al. 2014). Photometry for the Fundamental Plane
 579 sample was obtained by cross-matching with the 2MASS
 580 survey (Jarrett et al. 2000; Skrutskie et al. 2006).

581 Springob et al. (2014) produce peculiar velocity mea-
 582 surements with this sample by modelling the logarith-
 583 mic difference in observed and cosmological distances to
 584 each galaxy as a function of the logarithmic difference
 585 between their observed effective radii and the effective
 586 radii predicted from the best-fit Fundamental Plane. For
 587 each galaxy one can compute the probability of it hav-
 588 ing a particular distance modulus by assuming a Gaus-
 589 sian probability distribution function (PDF) about the
 590 Fundamental Plane. However, this procedure is com-
 591 plicated by Malmquist bias and the selection function
 592 of the 6dFGSv data, particularly the magnitude limit.
 593 The presence of a magnitude limit cuts a slice through
 594 the Fundamental Plane, such that the PDF is no longer
 595 normalised. Because the magnitude limit is in appar-
 596 ent magnitudes, the portion of the Fundamental Plane
 597 that cannot be observed varies with distance, and so the

normalisation of the PDF for each galaxy also depends on distance. To counteract this effect, Springob et al. (2014) produced a calculation of this normalisation as a function of distance using simulations drawn from the best-fit 6dFGSv Fundamental Plane with a $J < 13.65$ limit.

In subsequent work by Qin et al. (2018), similar simulations reproducing the Fundamental Plane, selection function and methodology applied to the 6dFGSv data were used to measure the bulk flow. A significant offset between the measured and true bulk flows in the simulations was identified in the direction directly toward the southern celestial pole. It was found possible to remove this effect in the simulations (and subsequently the data) by recalculating the normalisation of the probability distribution for each galaxy using an ad-hoc, brighter, magnitude limit of $J < 13.217$. In this work we repeat this calculation, paying special attention to not only the bulk flow, but also the Hubble parameter in radial shells.

We start by generating 128 mock 6dFGSv surveys matching the methods in Magoulas et al. (2012) and Qin et al. (2019), which are then run through a reconstruction of the 6dFGSv pipeline using a magnitude limit of $J < 13.65$. Unlike previous works, the normalisation of the PDF for each galaxy is computed using numerical Monte-Carlo integration of the truncated 3D Gaussian PDF, rather than summing over simulations. This procedure was found to result in less noise and was far more reliable for computing an accurate value at large comoving distances where by design the number of galaxies available to compute the probability, even over 128 simulations, quickly falls to zero.

The bulk flow in each simulation was then computed using the η -Maximum Likelihood Estimator (Kaiser 1988; Qin et al. 2018), as was the weighted mean value of

$$\log_{10}(H_i) = \log_{10}\left(\frac{f_i c z_i}{d_i}\right). \quad (3)$$

in redshift bins, where $f_i = 1 + 1/2[1 - q_0]z_i - 1/6[1 - q_0 - 3q_0^2 + j_0]z_i^2$, z_i is the redshift of the galaxy, q_0 and j_0 are the acceleration and jerk parameters and c is the speed of light. Here, d_i is the luminosity distance to each galaxy, computed assuming $H_0 = 75 \text{ km s}^{-1} \text{ Mpc}^{-1}$. For comparison, the same quantities are computed for each simulation using the true luminosity distance and peculiar velocity of each simulated galaxy.

The results of this procedure are shown in Figures 4 and 5. Also plotted alongside are the results for the original 6dFGSv data. From the binned Hubble parameters, it is clear that the mocks with distance moduli computed using the 6dFGSv pipeline exhibit an outflow and do not lie on the expected $H_0 = 75 \text{ km s}^{-1} \text{ Mpc}^{-1}$

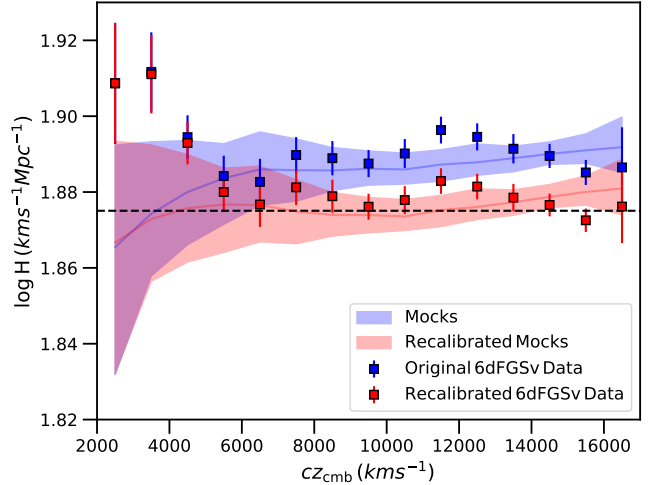


Figure 4. Measurements of the weighted mean Hubble parameter in redshift bins of width 1000 km s^{-1} from the 6dFGSv data (points) and simulations (band). The bands show the median value and 68% precentile region for the 128 mock realisations while the horizontal dashed line denotes the input value $H_0 = 75 \text{ km s}^{-1} \text{ Mpc}^{-1}$ used to compute the distance. We expect the Hubble parameter to be roughly constant with redshift and lie close to the input value. The blue band/points show the Hubble parameter using the original 6dFGSv methodology with a magnitude limit of $J < 13.65$ for the Malmquist bias correction. The red band/points show the recalibrated results using $J < 13.38$, which clearly reduces the bias seen in the mocks. Though high, the 6dFGSv data for $cz_{\text{cmb}} < 5000 \text{ km s}^{-1}$ are still within the 95% region computed from the simulations.

line. The distribution of these same mocks matches the data, which leads us to conclude the same is likely true for the data too. This trend is not obvious without the presence of simulations (and so not highlighted previously), particularly because cosmic variance at $cz_{\text{cmb}} < 5000 \text{ km s}^{-1}$ seems to be scattering the observed Hubble parameters high in the data.

The effect on the bulk flow is particularly pronounced. It was found by Qin et al. (2018) that the measured bulk flow in the simulations is biased quite negatively in the direction of the southern celestial pole compared to the bulk flow known to exist in the simulations. Although the ‘true’ bulk flow in the 6dFGSv is not known and can only be estimated, the measured value is consistent with the biased mock results, leading us to conclude that the data is similarly biased.

As with the previous work by Qin et al. (2018), we correct for this problem by modifying the magnitude limit used in the Malmquist bias correction/normalisation of each galaxy’s PDF. By iterating, a magnitude limit of $J < 13.38$ was found to produce binned Hubble parameters that are flat with redshift while also substantially reducing the difference between the adjusted and mea-

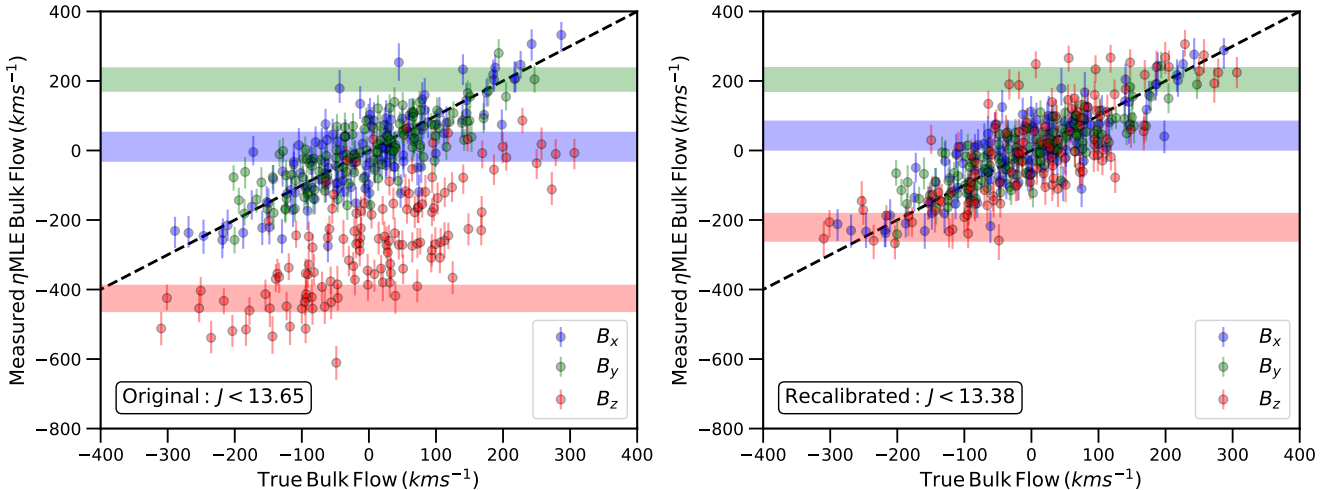


Figure 5. Measurements of the bulk flow in each direction from 6dFGSv mocks (points) and data (bands) using the ηMLE method of Qin et al. (2018). For each simulation we plot the measured maximum likelihood bulk flow against the true bulk flow calculated by averaging over the true peculiar velocity of each galaxy. The true bulk flow for the data is not known *a priori* and so the measurement is included as a horizontal band. In both cases error bars/regions denote the equal likelihood bounds encapsulating 68% of the posterior. The left hand panel shows the results using the original 6dFGSv methodology and $J < 13.65$ magnitude limit for the Malmquist bias correction/PDF normalisation. The right hand panel shows the recalibrated results using $J < 13.38$. The recalibration removes the strong negative bias in the bulk flow in the direction of the south celestial pole (z -axis in this coordinate system) seen in the simulations and believed to also be present in the data.

sured bulk flows. The results of applying this limit to the mocks and data are shown in Figs. 4 and 5. The small differences between the optimal value found here and that used in Qin et al. (2018) are likely the result of the more rigorous calculation of the normalisation using numerical integration adopted in this work.

We believe this re-calibration to be robust and so use the updated 6dFGSv data in *Cosmicflows-4*. The source of the discrepancy between the magnitude limit used to construct the simulations and the optimal value found for the Malmquist bias correction is unclear, but indicates a discrepancy between the best-fit 6dFGSv Fundamental Plane (from which the simulation apparent magnitudes are derived) and the assumed magnitude limit of the data. It is not inconceivable that the true magnitude limit of the 6dFGSv data is in reality brighter than the nominal selection function, particularly in light of the other aspects of the sample selection required to go from the 2MASS photometry and 6dFGS spectra to the Fundamental Plane sample, and then again to the peculiar velocity sample. However, there may be more to the picture. A preferable solution would be to perform a joint fit for the Fundamental Plane parameters and peculiar velocities simultaneously, again validated against simulations, however such an analysis is beyond the scope of the current work.

The systematic problem as a function of morphological type identified by Tully et al. (2016) remains in the revised bias adjusted 6dFGSv distances. Candidates in

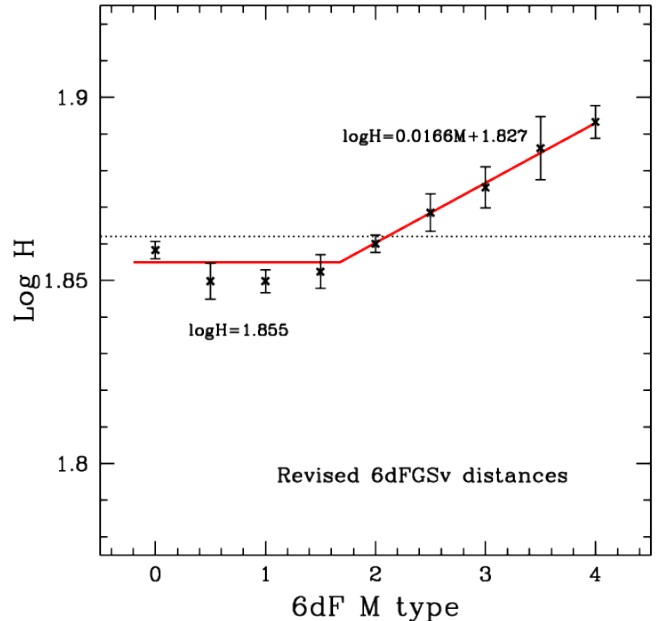


Figure 6. Trend in values of $\log H_i = \log(fV_i/d_i)$ with morphological M type. Galaxies with $M > 2$ increasingly manifest the properties of disk systems.

the 6dFGSv compilation are given a morphology M description, with $M=0$ for ellipticals, $M=2$ for lenticulars, and $M=4$ for spirals. As seen in Figure 6, there is a clear drift in $\langle fV_i/d_i \rangle$ with M , where V_i and d_i are individual galaxy velocities and distances and f is defined in

705 association with Eq. 3. The drift is in the sense that d_i
 706 values are increasingly measured too low with increasing
 707 M.

708 This situation is not too surprising given that the Funda-
 709 mental Plane pertains to galaxy bulges. The admix-
 710 ture of disk contributions evidently creates a systematic.
 711 The revisions discussed above to 6dFGSv distances has
 712 not addressed this morphology-related problem. Adjust-
 713 ments are made to distances that statistically counter
 714 the trend seen in Fig. 6. Only the fitting parameters
 715 are changed from the adjustments made in Tully et al.
 716 (2016). The distance moduli accepted into *Cosmicflows-*
 717 *4* incorporate both the revised bias corrections and the
 718 morphological corrections described in this section.

719 4.2. FP with SDSS Photometry and Spectroscopy

720 A new addition to the *Cosmicflows* program is the
 721 Sloan Digital Sky Survey (SDSS) peculiar velocity cat-
 722 alog (Howlett et al. 2022). Containing a total of 34,059
 723 objects, it is currently the largest single source of extra-
 724 galactic distance measurements available. It also con-
 725 tributes, along with a modest number of supernova ob-
 726 servations, the most distant objects in the *Cosmicflows-*
 727 *4* catalogue, extending up to a maximum CMB-frame
 728 redshift of $z_{\text{CMB}} = 0.1$. These measurements were made
 729 by combining public photometric data from SDSS Data
 730 Release 14 (Abolfathi et al. 2018) over a contiguous
 731 $\sim 7,000 \text{ deg}^2$ area with existing spectroscopic H α and
 732 velocity dispersion measurements (Thomas et al. 2013).

733 The full catalogue is magnitude limited to $10.0 \leq$
 734 $m_r \leq 17.0$ and velocity dispersion limited to $\sigma >$
 735 70 km s^{-1} . The selection of the sample also included a
 736 number of additional cuts on the surface brightness pro-
 737 files, concentration index, color, axial ratio, H α equiv-
 738 alent width and visual morphology to ensure a clean
 739 sample of elliptical galaxies is retained. As part of this
 740 process, cuts were applied using the morphological M-
 741 type (Tempel et al. 2011) before fitting of the Funda-
 742 mental Plane, so no correction of the form seen in Fig. 6
 743 for the 6dFGSv sample is required for the new SDSS
 744 data.

745 After data cuts, the sample was first fit using the 3D
 746 Gaussian Fundamental Plane model. Then, for each
 747 galaxy, the PDF of the logarithmic distance ratio be-
 748 tween cosmological and observed comoving distances
 749 was obtained. The normalisation of this PDF is set by
 750 integrating over the portion of the Fundamental Plane
 751 within which each galaxy would be observable at a given
 752 cosmological distance, and hence encodes the selection
 753 bias. Larger proposed distances for each galaxy end up
 754 being up-weighted to account for the increased cosmo-
 755 logical volume in which a galaxy could be found, and

756 the lower sample completeness at those distances. Pre-
 757 vious work (i.e., (Springob et al. 2014)) computed this
 758 normalisation using Monte-Carlo simulations, which re-
 759 quires assuming the same normalisation for each galaxy.
 760 However, Howlett et al. (2022) demonstrated it can also
 761 be computed numerically, which makes the calculation
 762 much faster and allows one to use a different normalisa-
 763 tion for each object. The mean, standard deviation and
 764 skew of each PDF was used to describe the full PDF of
 765 each galaxy.

766 Using cosmological simulations of the SDSS data and
 767 selection function, Howlett et al. (2022) demonstrated
 768 the measurements were unbiased as a function of red-
 769 shift and absolute magnitude. However, they did iden-
 770 tify a bias between the distance and group richness. This
 771 bias arises from a correlation between the mean sur-
 772 face brightness of galaxies in the sample and their cor-
 773 responding group richness, possibly hinting at intrinsic
 774 correlations in the Fundamental Plane due to a fourth
 775 unmodelled parameter such as stellar age. This group
 776 properties bias was corrected in the catalog by fitting
 777 separate Fundamental Planes to subsamples of the data
 778 as a function of group richness. These ‘corrected’ dis-
 779 tance measurements are the ones used in this work.

780 Calibration of the zero-point in the SDSS PV cata-
 781 logue is made difficult due to the small sky area. In
 782 Howlett et al. (2022) this calibration was performed
 783 by cross-matching to groups containing galaxies with
 784 *Cosmicflows-3* distances. The use of groups was found
 785 to be important considering the group richness bias dis-
 786 cussed above, although consistency with *individual* mea-
 787 surements in the two catalogs was also demonstrated as
 788 long as the ‘uncorrected’ SDSS distances were used.

789 4.3. Combining all Fundamental Plane distances

790 Just as multiple acquisitions of a distance to a spiral
 791 galaxy with photometry and rotation curve information
 792 are highly correlated, so it is the case with multiple ap-
 793 plications of the Fundamental Plane to early type galax-
 794 ies. Hence, as an initial step we bind all the Fundamen-
 795 tal Plane sub-samples into a joint sample. The same
 796 methodology as discussed in §3.4 is adopted to combine
 797 the distances of the FP catalogs of this study: “SDSS”,
 798 “6dFGSv”, “smac”, “enear” and “efar”.

799 As noted at the introduction of §4, there is only the
 800 tiniest overlap of 41 cases between “6dFGSv”, which is
 801 entirely restricted to negative declinations, and “SDSS”,
 802 which is limited to the north galactic and celestial
 803 pole caps, dipping slightly into the celestial south to
 804 $\delta = -3.7^\circ$. Consequently, the “smac”, “enear” and
 805 “efar” samples play the important roles of providing
 806 scaling links between the two large samples. Specifi-

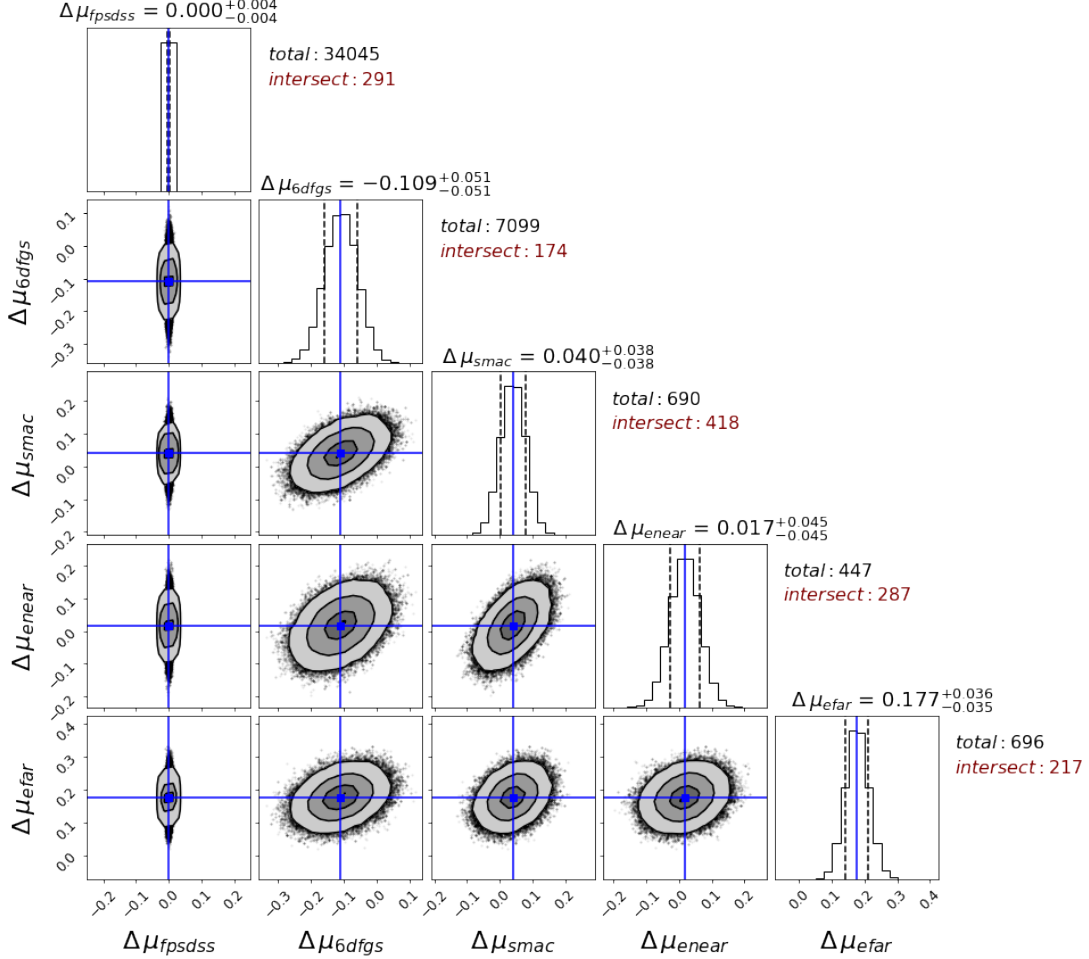


Figure 7. The posterior distribution of the optimized zero points of FP catalogs with respect to “SDSS”. Each panel covers ± 0.25 mag about the center of distribution. Other details are as in Figure 3.

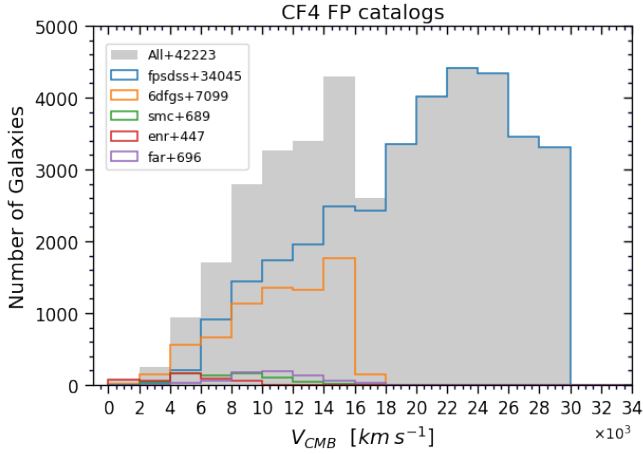


Figure 8. Cumulative histogram of FP targets with systemic velocity and a breakdown by sub-sample as given by the legend.

cally, “smac” provides 118 and 90 links with “SDSS” and “6dFGSv” respectively, “enear” provides 75 and 41

respectively, and “efar” provides 28 and 41 respectively. Collectively, these three smaller samples provide 367 overlaps with “SDSS” and 200 overlaps with “6dFGSv”.

The 3.5σ rejection criterion is used to identify two outliers in “enear”, one in “smac” and 17 in “6dFGSv” sub-samples. These cases are removed prior to the subsequent calculations.

With the interlacing of FP samples, the “SDSS” distances are taken as the reference of comparisons, whence $\Delta\mu_{SDSS} = 0$ by our convention. The posterior distribution of the offset parameters ($\Delta\mu_s$) are explored with our MCMC procedure in a similar fashion to that explained in §3.4. Figure 7 illustrates the posterior distributions of the moduli offsets of “6dFGSv”, “smac”, “enear” and “efar” sub-samples from “SDSS”. It is to be appreciated that, while the zero-point of the SDSS sample was set to be in approximate agreement with *Cosmicflows-4* distances (Howlett et al. 2022), it remains to receive further adjustment in the coupling with the full complement of methodologies described further along. In

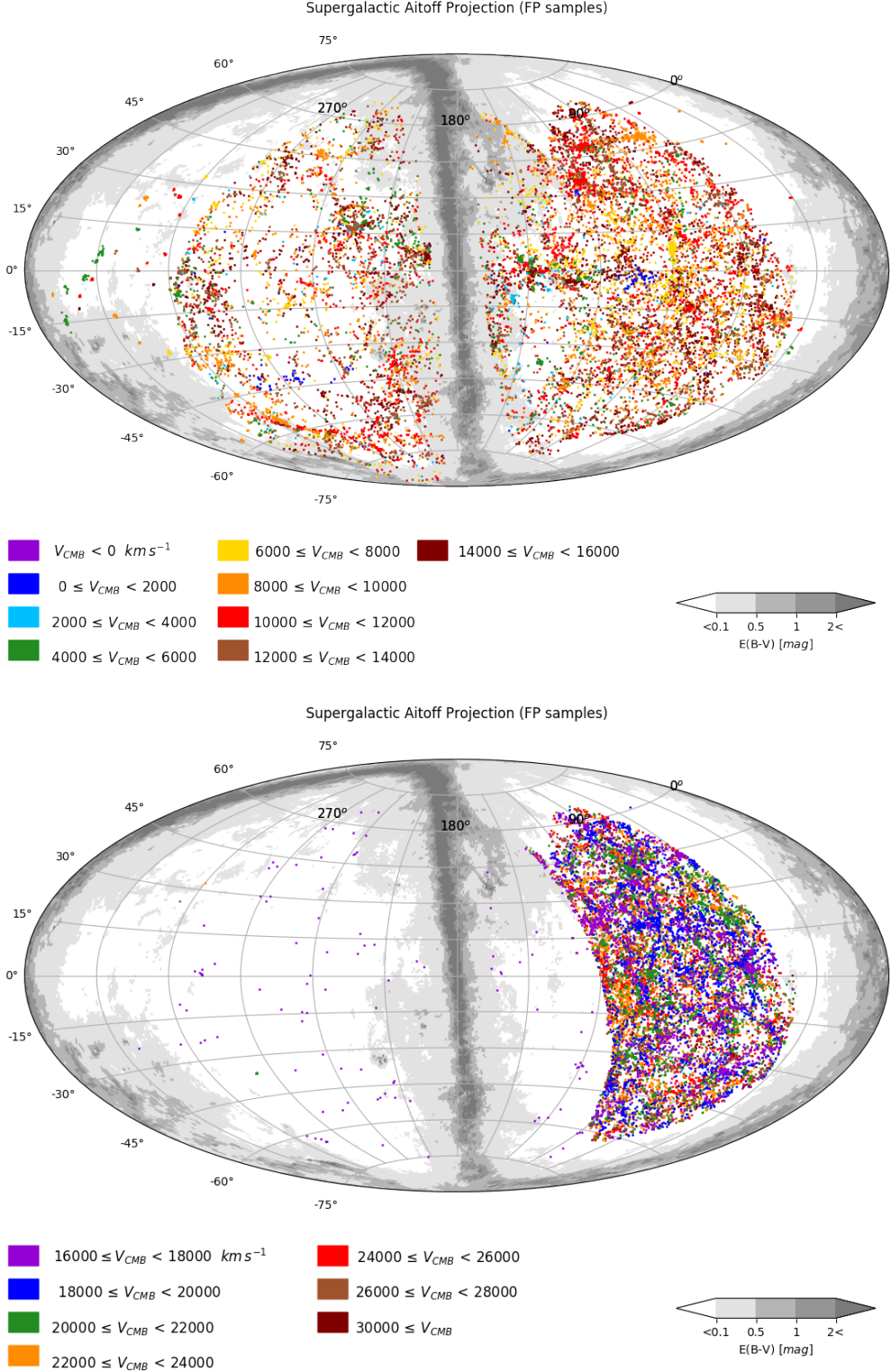


Figure 9. Aitoff projections in supergalactic coordinates of the distribution of the ensemble of FP samples. Top panel: 16744 cases with $V < 16,000 \text{ km s}^{-1}$. Bottom panel: 25479 cases with $V > 16,000 \text{ km s}^{-1}$. Colors relate to systemic velocities of the group of a galaxy as given in the table below the map. Milky Way extinction levels are cast in shades of grey. The dense roughly vertical swaths of objects in the north supergalactic hemisphere in both panels lie in the SDSS declination band. Contributions from the 6dFGSv sample lie to the left of the SDSS sample in the top panel.

particular, the union between methodologies afforded by group memberships will be exploited.

A histogram of the distribution of all FP measurements with velocity is shown in Figure 8. The “6dFGSv” and “SDSS” contributions are comparable at $V_{cmb} < 16,000 \text{ km s}^{-1}$. Only SDSS information is available between $16,000 \text{ km s}^{-1}$ and the sample cutoff at $z = 0.1$. Figure 9 shows the distribution of the galaxies with FP measurements on the sky, split into two panels for those above and below $16,000 \text{ km s}^{-1}$.

5. SURFACE BRIGHTNESS FLUCTUATION DISTANCES TO EARLY TYPE GALAXIES

In predominantly ancient stellar systems, the brightest stars lie on the red giant branch where stellar envelopes inflate and hydrogen burning occurs in shells around inert helium cores (Salaris & Cassisi 2005; Serenelli et al. 2017). The very brightest of these stars, at the “tip” of the red giant branch, are precursors to the onset of core helium burning and a restructuring of the star onto the horizontal branch. The passband dependence of the luminosity of a star at the tip varies with metallicity, with enhanced molecular line blanketing pushing emission redward. At solar or super-solar metallicities, the stars at the tip of the red giant branch peak in luminosity around $2 \mu\text{m}$. The robustly-characterized luminosity of the onset of core helium burning, and the fact that it is very bright, have been exploited to measure galaxy distances.

In galaxies that can be resolved into individual stars, the preferred distance measurement methodology uses properties of the tip of the red giant branch, to be discussed in a later section. For more distant targets, the stars blend, but the surface brightness appears mottled because of the Poisson statistics in the number of stars per resolution element, creating surface brightness fluctuations (SBF) (Tonry & Schneider 1988). The signal from the stellar fluctuations in the spatial Fourier power spectrum diminishes with distance as $1/d^2$, making it possible to measure galaxy distances with high accuracy with simple single-epoch imaging, which distinguishes SBF from other distance measurement techniques that rely on temporal monitoring (Cepheids and supernovae) or spectroscopic observations (e.g., FP and TFR).

5.1. Sources of SBF Measurements

We have gathered SBF distances for 508 galaxies based on five sources of SBF measurements. Two of these sources already found a presence in the earlier *Cosmicflows* compilations. Tonry et al. (2001) pioneered the methodology with observations from the ground at the optical *I*-band. That program targeted 300

E/S0 galaxies including essentially all E galaxies within $2,000 \text{ km s}^{-1}$ and a sampling out to $4,000 \text{ km s}^{-1}$. The other earlier source of SBF distances was the HST study of E/S0 galaxies in the Virgo and Fornax clusters (Mei et al. 2007; Blakeslee et al. 2009, 2010). The exceptional spatial resolution of HST resulted in distance measurements with sufficient accuracy to resolve the three-dimensional structure of the Virgo Cluster, distinguishing the M, W, and W' background galaxy groups, and to provide an accurate differential distance between the Virgo and Fornax clusters.

Now with *Cosmicflows-4* we add SBF distance information from two new sources. The first of these (Cantiello et al. 2018a) is an extension of the HST Virgo Cluster study derived from the u^*, g, i, z imaging Next Generation Virgo Cluster Survey carried out with the Canada-France-Hawaii Telescope (Ferrarese et al. 2012). Our knowledge of the Virgo Cluster environs and, particularly, of the separation of the W' group 50% farther away in projection and the W and M structures twice as far away, are given improved clarity with this enhanced distance compilation.

The second new SBF source, infrared SBF with the HST WFC3/IR camera, is a harbinger of a particularly promising improvement to the SBF methodology (Jensen et al. 2021). The wide field of view and improved sensitivity of WFC3/IR over earlier ground-based and NICMOS IR observations makes it an optimal instrument for SBF measurements. Red giant stars are particularly bright in the near-IR, making IR SBF much brighter and easier to measure than at optical wavelengths, especially from space where the sky background is greatly reduced. Jensen et al. (2015) established the calibration for SBF in the $F110W$ and $F160W$ filters using observations of 16 Virgo and Fornax galaxies. As discussed in Blakeslee et al. (2021), these IR SBF distances are tied to the *I*-band SBF observations (Blakeslee et al. 2009), the Cepheid distances to Virgo and Fornax, and the LMC distance modulus of 18.477 (Pietrzynski et al. 2019).

The HST $F110W$ SBF observations reach a distance of 80 Mpc in a single orbit, with an observational error of 4–5% (Blakeslee et al. 2021; Jensen et al. 2021). A number of different WFC3/IR $F110W$ programs have now been mined for usable observations. Two of these programs targeted galaxies specifically for SBF distance measurements. The program MASSIVE seeks to understand the stellar dynamical properties and central black hole masses of massive galaxies within ~ 100 Mpc (Ma et al. 2014). This study includes the determination of 41 high-quality IR SBF distances. A second targeted SBF study measured distances to 19 early-type type-Ia

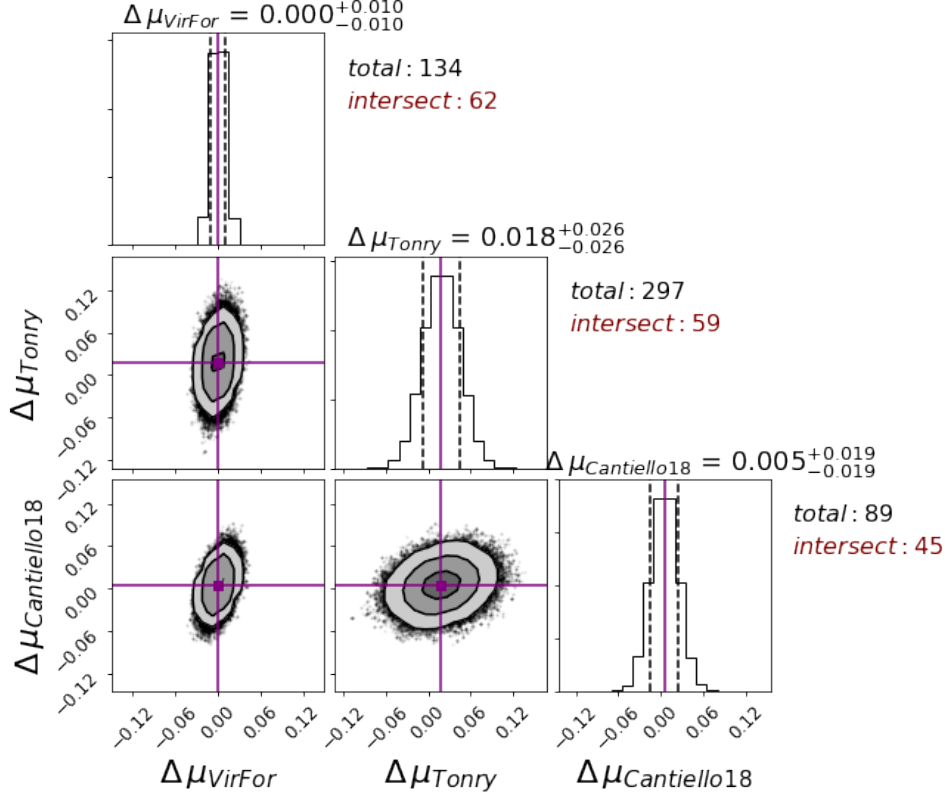


Figure 10. The posterior distribution of the optimized zero points of SBF catalogs with respect to the “Virgo-Fornax” catalog. Each panel covers ± 0.15 mag about the center of distribution. Other details are as in Figure 3.

supernova host galaxies (Milne et al. 2022; Garnavich et al. 2022, in prep). These data sets, along with independent observations of NGC 4874 in Coma (Cho et al. 2016; Bartier et al. 2017) and NGC 4993, the 2017 gravitational wave event host (Cantiello et al. 2018b), sum to a total of 62 galaxies out to 100 Mpc for which high-precision distances are now known.

5.2. Combining SBF sub-samples

There is significant overlap between only three of the four SBF sub-samples. The new IR SBF contribution has an overlap of only 8 targets with Tony. The corner plot for the three SBF sub-samples that can be compared is seen in Figure 10. The Virgo/Fornax collection based on HST optical band observations is taken as the reference. Whereas with the TF and FP studies galaxy-group comparisons help reduce errors, in the case of SBF the galaxies are relatively nearby and the individual accuracies are greater so comparisons are strictly galaxy-galaxy. The integration of the full four SBF contributions awaits the global MCMC compilation of all methodologies.

Figure 11 is a histogram of the cumulative SBF sample dependence on systemic velocity, with a breakdown by source.

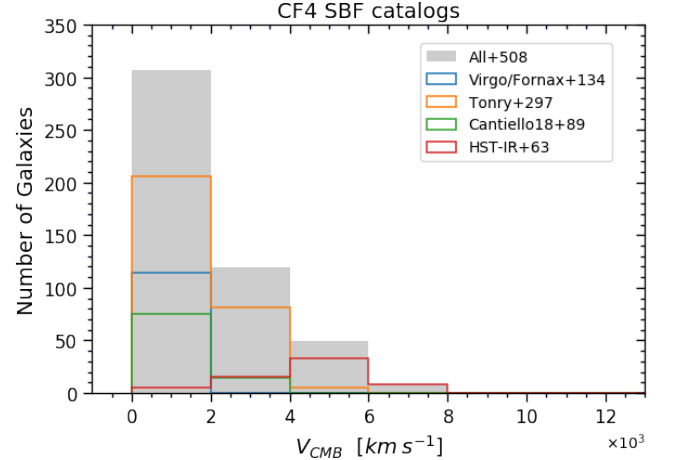


Figure 11. Cumulative histogram of SBF targets with systemic velocity and a breakdown by sub-sample as given by the legend.

6. DISTANCES TO THE GALAXY HOSTS OF SUPERNOVAE

There are two predominant types of supernovae: those associated with stars with degenerate cores (type Ia) and those associated with stellar core collapse (type II). The former are well established as providing a methodology

for measuring distances with high accuracy. The latter have seen less use and have reduced accuracy per event. We give attention to samples of both.

6.1. Distances to the Galaxy Hosts of Type Ia Supernovae

Supernovae of Type Ia (SNIa) arise in binary systems where at least one of the stars is a white dwarf. The path, or possibly paths, resulting in explosions is not resolved, with the two most discussed alternatives being, alternatively, single-degenerate models where matter from a companion accretes onto a white dwarf, or double degenerate models where two white dwarfs merge (Maoz et al. 2014). In spite of this uncertainty in the physical mechanism, the minimal dispersion in the absolute luminosities of Type Ia supernovae after a calibration based on post-maximum decline rate (Phillips 1993) can be exploited to measure galaxy distances with high accuracy. The events are sufficiently bright that SNIa at $z < 0.1$ can be discovered and monitored with moderate sized telescopes. This methodology can provide distances with 2 to 3 times the accuracy of TF and FP with considerably greater reach. Supernovae are serendipitous events, though, and the number of well studied occurrences remains small.

Modest samples of SNIa were included in earlier releases: 308 cases in *Cosmicflows-2*, increased to 389 in *Cosmicflows-3*. Here, those samples are augmented by contributions from four new sources, more than doubling the available sample to 1008 SNIa events within $z = 0.1$. Core collapse supernovae (SNII) are proving to be useful distance tools also, although not with the same accuracy. A limited sample of SNII will be discussed in §6.2.

The new samples beyond those of *Cosmicflows-3* include 235 hosts from the Lick Observatory Supernova Search (Ganeshalingam et al. 2013), 137 hosts from the first release of the Carnegie Supernova Project (Burns et al. 2018), 669 hosts from the collection by Stahl et al. (2021), 597 hosts in the PantheonPlus compilation (Scolnic et al. 2021; Brout et al. 2021), the 560 late-type hosts in the largely overlapping and augmented Pantheon+SH0ES sample (Riess et al. 2022), 134 hosts of SNIa with spectral "twin" properties by the Nearby Supernova Factory (Boone et al. 2021), and 89 hosts of events studied at infrared bands (Avelino et al. 2019).

There are considerable overlaps between these and the earlier contributions, as is evident if the contributions are summed. Diverse light curve fitters are involved. Selection cuts differ between programs and analyses could involve different photometry in different passbands but it is reassuring that alternate distance measurements to

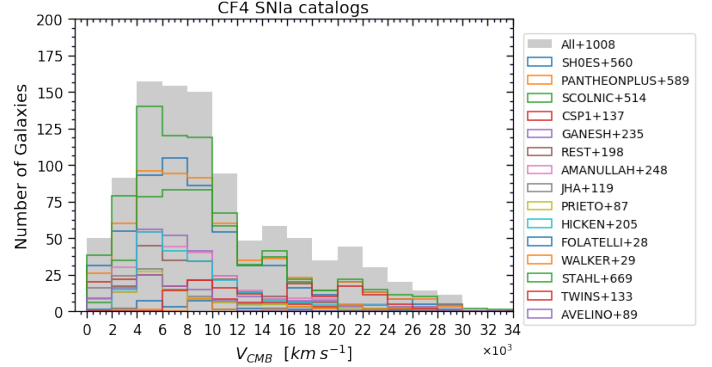


Figure 12. Cumulative histogram of SNIa targets with systemic velocity and a breakdown by sub-sample as given by the legend.

the same events are in agreement. For 200 pairwise comparisons of multiple distance entries to the same SNIa the weighted average difference of 0.063 mag in the modulus was found, about 3% in distance. The agreement is considerably less good in the distance estimates to multiple SNIa in the same host. Twenty-one hosts have measurements for at least 2 SNIa events, with three such events in NGC 3417 and four in NGC 1316 in the Fornax Cluster. To avoid issues related to differences in analysis procedures and zero point scaling we consider just the thirteen hosts with multiple events in the SH0ES study (Riess et al. 2022). The rms scatter of 0.278 mag corresponds to an uncertainty of 13.6% in distance. This large scatter is puzzling, especially since peculiar velocities are removed as a factor with events in a common host. By comparison, Avelino et al. (2019) and Boone et al. (2021) contend that the scatter they find with conventional light curve fitters at optical bands correspond to $\sim 7\%$ in distance, with improvements to 5% with inclusion of infrared photometry or spectral matching ("twins embedding") respectively.

A histogram of the distributions in velocities of the SNIa sub-samples is shown in Figure 12. The 15 SNIa samples are merged in a manner analogous to that discussed in §3.4. The corner plot of moduli offsets following from the MCMC analysis is seen in Figure 13. The zero point scaling is set to that provided by the SH0ES sample although, as with all the individual methodologies, the absolute scaling is subject to revision with the merging of all available material. Figure 14 illustrates the distribution of SNIa on the sky along with the SNII and SBF contributions. Under sampling in the celestial south accounts for the under representation of events at supergalactic longitudes $180^\circ - 270^\circ$ to the left of the zone of obscuration in the plot. Concentrations of SBF contributions can be seen at the positions of the Virgo



Figure 13. The posterior distribution of the optimized zero points of SNIa catalogs with respect to the SHOES distance moduli. Each panel covers ± 0.15 mag about the center of distribution. Other details are as in Figure 3.

and Fornax clusters, at right central and lower left respectively.

6.2. Core collapse Type II supernovae

Although SNII vary intrinsically by more than two magnitudes, the underlying events are better understood than is the case with SNIa and their luminosities correlate with observable properties. More luminous

SNII have higher photospheric expansion velocities (Hamuy & Pinto 2002) and are bluer. Colors are a monitor of extinction. In *Cosmicflows-4* we include a sample of 96 SNII in 94 hosts studied by de Jaeger et al. (2020b,a). The 1σ scatter about the Hubble diagram is $\sim 15\%$ in distance, about a factor two worse than realized with SNIa.

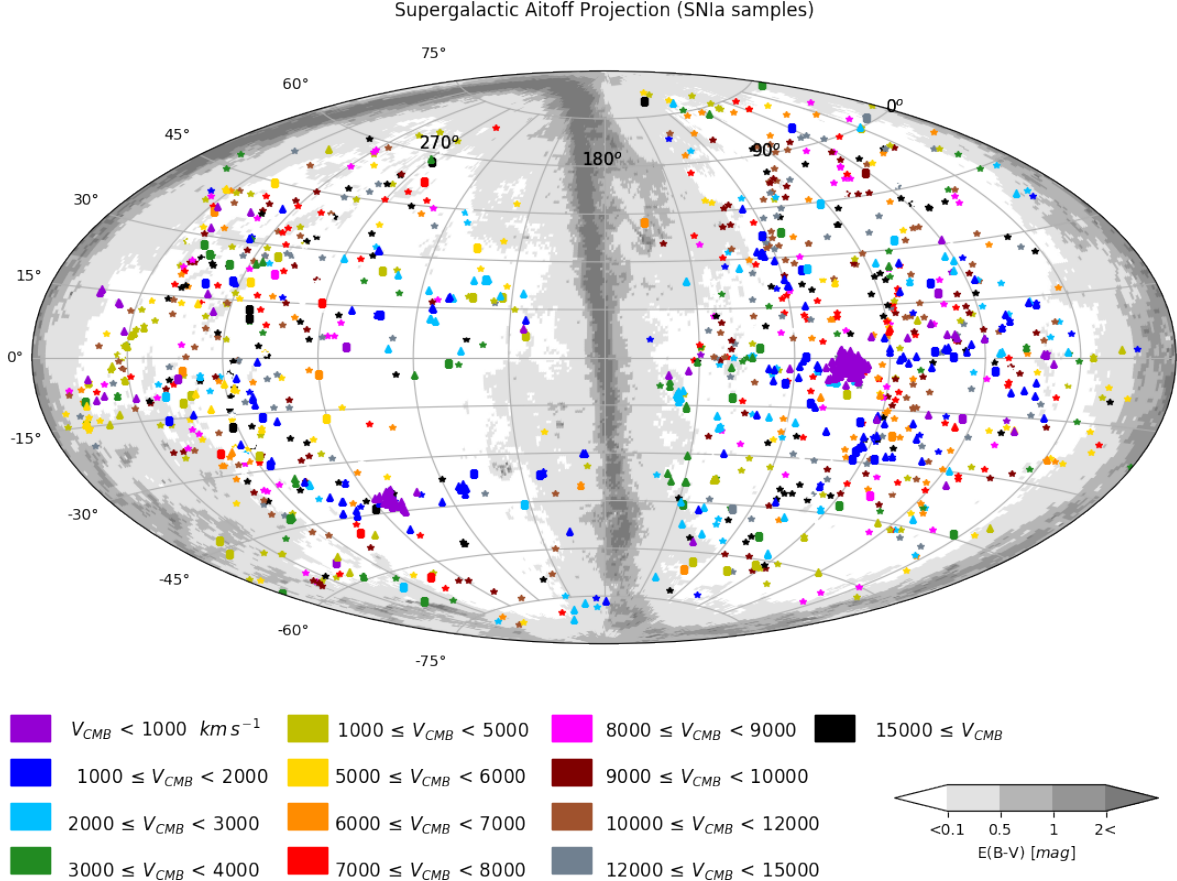


Figure 14. An aitoff projection in supergalactic coordinates of the distribution of the ensemble of 1008 SNIa (asterisks), 94 SNII (squares) and 480 SBF (triangles) galaxies. Colors relate to systemic velocities of the group of a galaxy as given in the table below the map. Milky Way extinction levels are cast in shades of gray. There are concentrations of SBF targets in the Virgo Cluster at right-center and the Fornax Cluster at lower left.

7. TIP OF THE RED GIANT BRANCH

The Tip of the Red Giant Branch (TRGB) method for acquiring distances has two particularly resonant impacts on our program. Relative accuracies (not accounting for zero point issues) are typically at the level of 5% with Hubble Space Telescope observations. On the one hand, given an absolute calibration, the numerous measurements now available with overlaps with other methodologies play an important role in setting the absolute scale for extragalactic distances (Freedman et al. 2019; Anand et al. 2022). On the other hand, the dense coverage of sources locally affords unprecedented information on a multitude of research interests. The current edition of *Cosmicflows* provides TRGB distances to 489 galaxies (Anand et al. 2021).

TRGB and the SBF procedure discussed in §5 have closely related physical bases. With SBF, the brightest stars on the red giant branch are unresolved and distances are inferred from the statistical properties of im-

age mottling. With TRGB the individual brightest red giant stars can be isolated and their brightness measured. There is extensive experience with use of the TRGB as a distance tool (Da Costa & Armandroff 1990; Lee et al. 1993; Madore & Freedman 1995; Méndez et al. 2002; Makarov et al. 2006; Rizzi et al. 2007; Wu et al. 2014; McQuinn et al. 2017; Jang & Lee 2017; Beaton et al. 2018).

In practise, SBF and TRGB are most effective in two distinct regimes. There are concerns with contamination from young populations and metallicity effects that are addressed in different ways. In the case of SBF, the most stable candles are high surface brightness, very old, and high metallicity systems, with relative intrinsic magnitude constancy in the infrared. In the case of TRGB, the optimal target stars have low metallicity and are observed near to $900 \mu\text{m}$ where metallicity and age effects are minimal. Such stars are best sought in the halos of galaxies where there is minimal extinction or crowding or contamination from young populations.

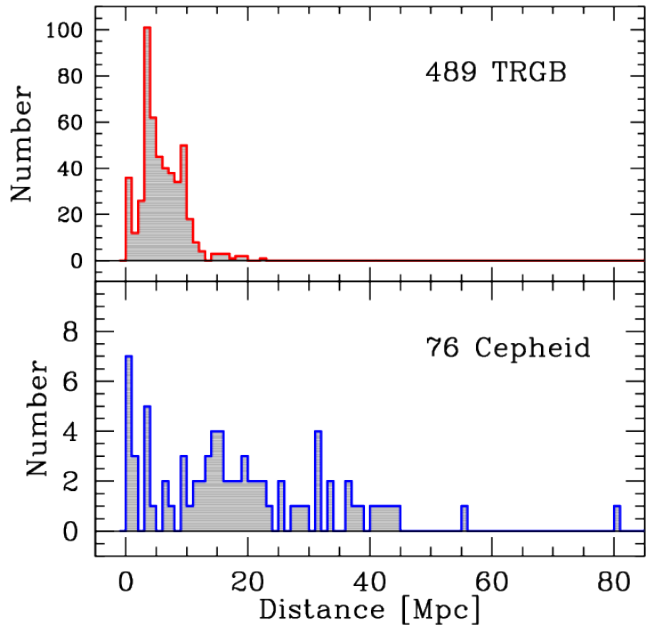


Figure 15. Distribution in distance of the TRGB and Cepheid Period-Luminosity samples.

While several groups have been involved with TRGB studies, with a partial literature given above, all results reported in *Cosmicflows* have been drawn from data in the HST archives and analyzed in a uniform way with our standard procedures (Jacobs et al. 2009; Anand et al. 2021). Proceeding from *Cosmicflows-2* to -3 to -4 , our collection of TRGB distances has grown from 297 to 384 to 489. Ninety percent of galaxies brighter than $M_B = -13$ within 10 Mpc now have distance estimates with 5% accuracy. This material has given rise to population studies of individual systems (Makarova et al. 2017; Karachentsev et al. 2017), to studies of the grouping properties of galaxies (Kourkchi & Tully 2017), and to studies of local filamentary structure and motions (Shaya et al. 2017; Anand et al. 2019).

The histogram of TRGB candidates with systemic velocity is seen in Figure 15. Given that most of the TRGB systems are within 10 Mpc because of the single orbit capabilities of HST, these candidates are mostly to be found in the restricted sector of the sky of our home Local Sheet (Tully et al. 2008).

The zero point of our TRGB distances had been established in our previous publications with the study by Rizzi et al. (2007). That calibration followed from the identification of the Horizontal Branch in five Local Group galaxies (Sculptor, Fornax, and NGC 185 spheroidals, the irregular IC 1613, and the spiral M33) assuming the Horizontal Branch absolute magnitude found by Carretta et al. (2000) and the implications

for the absolute magnitude of the TRGB drawn from those systems. More recent calibrations of the TRGB zero point have lead to some dispute (Jang & Lee 2017; McQuinn et al. 2017; Freedman et al. 2019; Yuan et al. 2019; Freedman et al. 2020). It is a specific concern that the stellar trigonometric parallax underpinning of Horizontal Branch absolute magnitudes, and hence the entire Population II distance ladder, is a product of Hipparcos satellite observations from the previous millennium. Information from Gaia satellite is emerging that indicate that a zero point re-scaling is in order. Attention will be given to this matter in §10.2.

8. CEPHEID PERIOD LUMINOSITY RELATION

The Cepheid Period Luminosity Relation (CPLR) or Leavitt Law (Leavitt & Pickering 1912) has been considered the gold standard as a method for measuring absolute galaxy distances. We accept a combined sample of 76 systems into *Cosmicflows-4*. Our reference compilation of 40 objects is that given by Riess et al. (2016, 2019, 2022), see also Yuan et al. (2020, 2021), assuming the Detached Eclipsing Binary distance modulus of $\mu_{LMC} = 18.477 \pm 0.004$ (stat) ± 0.026 (sys) of Pietrzynski et al. (2019) ($d_{LMC} = 49.59 \pm 0.09$ Mpc). We also use 23 non-overlapping systems observed in the course of the HST key project to measure H_0 (Freedman et al. 2001) shifted to the LMC distance given above. We include 12 systems all within ~ 3 Mpc observed from ground based observatories and reported by Bhardwaj et al. (2016) and the Araucaria collaboration (Zgirski et al. 2017), with scales set to our LMC distance. The final case observed with HST and on our LMC scale is NGC 6814 (Bentz et al. 2019). A histogram of the measured distances of CPLR targets is given in Figure 15.

The absolute calibration of the CPLR remains a work in progress. Cepheid variables are young stars that tend to live in crowded, dusty environments. It remains to be resolved if there are metallicity dependencies. There are expectations of a more refined scaling once parallax information provided by Gaia is digested (Riess et al. 2021). Our final scaling with *Cosmicflows-4* will be reviewed in §10.

9. NUCLEAR MASERS

The fortuitous occurrence of a water maser in the nucleus of NGC 4258 is making an out-sized contribution to studies of the extragalactic distance scale because of the well defined geometry of the event (Humphreys et al. 2013; Reid et al. 2019). Observations of the positions, velocities, and accelerations of the maser signals can be modelled to give a direct geometric estimate of the angular-diameter distance of the galaxy without re-

course to information external to the system. The situation in the case of NGC 4258 is particularly favorable because the plane of rotation of the masers is almost edge-on and the very long baseline radio interferometric signals are strong. The measured distance modulus is 29.397 ± 0.032 , a formal error of only 1.5% in distance.

The occurrence in NGC 4258 is fortuitous indeed because extensive searches have, to date, only turned up five more cases that have warranted the attention leading to publication (Pesce et al. 2020). Uncertainties vary wildly (median $\sim 10\%$) because signals are weak and geometries are less favorable. Distances for all of these systems are included in *Cosmicflows-4* at their geometrically determined values. While non-geometric distances are subject to modification in the Bayesian analysis to follow, the maser distances (with associated uncertainties) are fixed.

10. ALL TOGETHER

In the sections above there have been discussions of the MCMC merging of sub-samples within discrete methodologies. In these cases, the analysis of targets in common have been made in separate studies. Perhaps there have been independent observations, or distinct analysis procedures, but the premise is that there should be consistency in distance measurements by the same technique. Scatter in multiple measures to the same galaxy should be (and are found to be) modest compared with the characteristic uncertainties in a method.

By contrast, distance information to a given galaxy by multiple methodologies is too rare to provide robust binding of the ensemble. For example, if among the early-type FP and a late-type TF samples there is a galaxy in common (there are 67 cases among a total of 55,000 possible) then the result from at least one of the two contributions is suspect, given probable type confusion. Then the overlaps involving SBF and supernovae of either types Ia or II are modest because these samples are modest. For the merging of these methodologies we must look to coincidences in group affiliations.

The 55,681 galaxies with distances by at least one of these five sources find their way into 37,838 groups, including groups of one. Some of the groups are well represented. For example, in the case of the Coma Cluster (Abell 1656; 1PGC 44715), there are 209 FP measures, 50 TF measures, 7 SNIa hosts and 2 SNII hosts. In the adjacent Leo Cluster (Abell 1367, 1PGC 36487) the numbers are 66, 49, 2 and 1, respectively. In the more distant Hercules Cluster (Abell 2147/51, 1PGC 56962) there are 193 FP contributions, 60 by TF, and 2 SNIa. In the nearby Virgo Cluster (1PGC 41220) we find 32 FP, 49 TF, an impressive 132 SBF, and 4 SNIa. Overall,

there are 694 groups with FP–TF intersections. SBF has 67 intersections with FP and 142 intersections with TF, cumulatively in 161 groups.

To this juncture TRGB, CPLR, and maser contributions have not been mentioned. These elements require special care because the targets are close by and the measurements are accurate enough to resolve their constituent groups. Indeed, attention needs to be paid to this concern with SBF and SNIa targets within $\sim 2000 \text{ km s}^{-1}$.

10.1. Merging TF, FP, SBF, SNIa, and SNII

Our procedure to achieve the union of the five methodologies, TF, FP, SBF, SNIa, and SNII, is conceptually the same as that described in §3.4 with application to each of the individual methodologies. The fundamental difference is that, whereas with the individual methodologies the bonding involves matching between galaxies, now the linkage units are galaxy groups. So, for example, the 42,254 galaxies with FP distances are bundled into 27,701 groups. The distance to a group is the weighted average of the moduli of all the FP measures in the group, with a statistical error given by the inverse square root of the sum of the weights.³ The velocity of the group is found by averaging over all known group members (not just those with distance estimates). In the case of TF, the 12,395 individual galaxies with distance estimates are bundled into 10,189 groups. With SBF, 425 individual galaxies lie in 227 groups. The 1008 individual SNIa hosts are found in 945 groups while the 94 SNII hosts are all in 94 separate groups.

As with the previous MCMC analyses of individual methodologies, one of the contributions is selected as a zero point reference. Here, we take the grouped SNIa sample as that reference. This choice is impelled by three factors. For one, the SNIa sample provides the best cross-reference overlaps with the numerically dominant FP and TF components. Also, there is utility in the greater accuracy of SNIa distances. Finally, it is most useful that the SNIa are widely dispersed and have great reach in distance. At the onset of the joint analysis, each methodology had been set on its own arbitrary zero point scale. For example, the SNIa scale is consistent internally with $H_0 \sim 71 \text{ km s}^{-1} \text{ Mpc}^{-1}$, the TF scale is consistent with $H_0 \sim 75 \text{ km s}^{-1} \text{ Mpc}^{-1}$, and FP, SBF, and SNII are intermediate. Now, all the methods will be brought to the same, but still arbitrary, zero point scaling within statistical uncertainties.

³ Individual weights are formed from the inverse square of *rms* uncertainties.

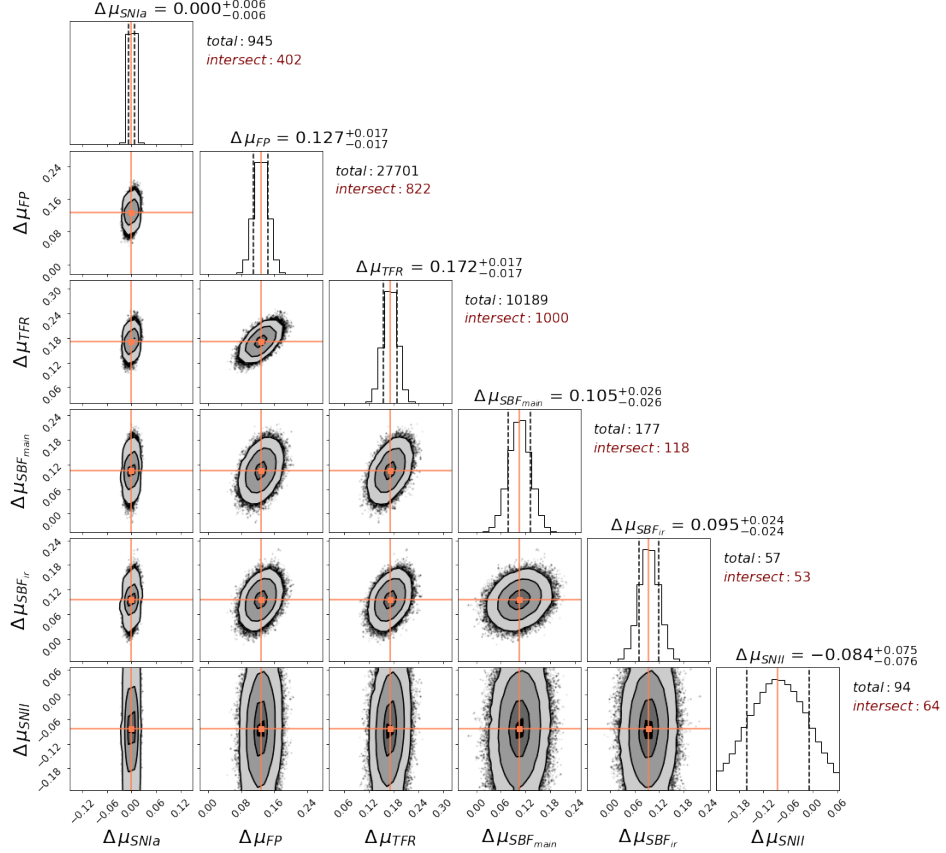


Figure 16. The posterior distribution of the optimized zero points of the group catalogs with respect to the “SNIa” catalog. Each panel covers ± 0.15 mag about the center of distribution. Other details are as in Figure 3.

The corner plot resulting from the MCMC merging of methodologies through joint group affiliations is seen in Figure 16. The constraints on the unions with FP and TF are robust because the intersections are numerous and can involve groups with many distance measurements. The constraints with SBF are reasonably good although intersections are limited because individual SBF measures have high accuracy. The constraints are weakest in the connection with the currently limited SNII methodology.

10.2. Zero point Calibration

The five methodologies that reach substantial distances have been merged to give coherent distances but on an arbitrary scale. It is through a matching of sources with TRGB or CPLR measurements that the ensemble is put on an absolute scale which manifests in an estimate of the Hubble Constant. Each of TRGB and CPLR are themselves anchored by other geometric techniques. Both take grounding in the nuclear maser distance of 7.576 Mpc to NGC 4258 that has a quoted uncertainty of 1.5% (Reid et al. 2019). A separate foundation for CPLR is the quoted 1% eclipsing binary distance of 49.59 kpc to the Large Magellanic Cloud (Pietrzynski

et al. 2019), the host galaxy for the largest coherent sample of cepheid variables. Both CPLR and TRGB take recourse in parallax measurements of appropriate stellar populations within the Milky Way. In the case of CPLR, 8 measurements come from HST WFC3 spatial scanning and 75 parallaxes are available from Gaia EDR3 (Riess et al. 2018, 2021). In the case of TRGB the parallax targets are abundant Population II stars that give specification of the Horizontal Branch (Carretta et al. 2000). Rizzi et al. (2007) identified the levels of the Horizontal Branch in five Local Group galaxies observed with HST (Fornax, Sculptor and NGC 185 dwarfs, IC 1613 and M33) to determine color dependent values for the absolute magnitude of the TRGB.

The Rizzi et al. (2007) TRGB scale can be compared with TRGB on the scale of Freedman et al. (2019). For 12 galaxies, there is the difference $\langle \mu_{rizzi} - \mu_{freedman} \rangle = -0.028 \pm 0.035$ with rms scatter ± 0.052 (Anand et al. 2022). This 1.5% difference in distances is not statistically significant but the Rizzi scale distances closer is consistent with the Anand et al. (2022) determination of a Hubble Constant value 0.9% higher than that by Freedman et al. (2019).

1324 There are indications that the Population II zero point
 1325 scaling will be altered somewhat as Gaia satellite Data
 1326 Release 3 (DR3) geometric parallaxes replace older Hip-
 1327 parcos parallaxes. The following presents a best effort
 1328 estimate of the Gaia informed re-scaling in advance of
 1329 access to Gaia DR3. We begin by recalling that the basis
 1330 for the Rizzi et al. (2007) calibration was the following
 1331 formula for the luminosities of stars on the Horizontal
 1332 Branch (HB) derived from Hipparcos satellite trigono-
 1333 metric parallaxes (Carretta et al. 2000)

$$M_V(HB) = 0.13([Fe/H] + 1.5) + 0.54 \quad (4)$$

1334 The same reference gave a related formula for the lumi-
 1335 nosities of the RR Lyrae stars (RR) that lie embedded
 1336 in the HB.

$$M_V(RR) = 0.18([Fe/H] + 1.5) + 0.5 \quad (5)$$

1337 Applied to the Large Magellanic Cloud, this reference
 1338 finds $\mu_{LMC} = 18.54 \pm 0.03 \pm 0.06$ (statistical and
 1339 systematic errors respectively). An updated version of Eq.5
 1340 based on parallaxes from the early release of Gaia DR3
 1341 (eDR3) is (Garofalo et al. 2022)

$$M_V(RR) = 0.33([Fe/H] + 1.5) + 0.63 \quad (6)$$

1342 and these authors find a distance to the LMC of $\mu_{LMC} =$
 1343 18.501 ± 0.018 . The change in the magnitude coefficient
 1344 at fiducial $[Fe/H] = -1.5$ implies RR Lyr stars fainter
 1345 by 0.06 mag (although note the greater metallicity de-
 1346 pendence). The application to the LMC would have the
 1347 LMC closer by 0.04 mag.

1348 Consider another study. Nagarajan et al. (2022) de-
 1349 rive new luminosity-metallicity and period-luminosity-
 1350 metallicity relations with luminosities in Wesenheit
 1351 magnitude units to negate reddening effects for 36 RR
 1352 Lyr in the Milky Way with eDR3 parallaxes and for RR
 1353 Lyr in 39 nearby dwarf galaxies, making a simultaneous
 1354 Bayesian fit to all Milky Way anchors and all RR Lyr
 1355 stars in each dwarf. They find an offset for the Milky
 1356 Way calibration stars from values obtained by Carretta
 1357 et al. (2000) $\mu_{gaia} - \mu_{hipparcos} = -0.048$ (without giving
 1358 an error). The subsequent distances obtained for the
 1359 nearby dwarfs (Nagarajan et al. 2022) can be compared
 1360 with our TRGB distance estimates with the Rizzi scal-
 1361 ing (Anand et al. 2021). In two of the cases, NGC 147
 1362 and NGC 185 with the RR Lyr information from Mon-
 1363 elli et al. (2017), the modulus discordances are almost
 1364 0.4 mag and the reported RR Lyr distances do not make
 1365 sense given the quality of the TRGB values. Discount-
 1366 ing these two cases, eight available comparisons give
 1367 $<\mu_{rizzi} - \mu_{rrl}> = 0.085 \pm 0.034$ with rms scatter ± 0.095 .

1368 Rather than bootstraps to TRGB luminosities
 1369 through RR Lyrae or the Horizontal Branch, there is

1370 the prospect of direct measurements of the luminosi-
 1371 ties of the brightest stars on the Red Giant Branch,
 1372 including dependencies on metallicity, from Gaia par-
 1373 allax measurements of large numbers of stars within the
 1374 Milky Way. A preliminary example is provided by the
 1375 study by Soltis et al. (2021) of the determination of the
 1376 TRGB magnitude for the ω Centaurus globular clus-
 1377 ter with Gaia eDR3 parallaxes. Their determination of
 1378 $M_{I,trgb} = -3.97 \pm 0.06$ is lower by ~ 0.08 from the Rizzi
 1379 et al. (2007) expectation.

1380 A common thread can be seen through the discussion
 1381 of this section. Distances following from the Hipparcos
 1382 based Rizzi et al. (2007) calibration are too great, al-
 1383 though the amplitude of the problem is uncertain. From
 1384 Garofalo et al. (2022), the revised scaling of RR Lyr
 1385 magnitudes and corresponding distance to the LMC sug-
 1386 gests a modification between 0.04 and 0.06 mag. From
 1387 Nagarajan et al. (2022), changes in distances to Milky
 1388 Way RR Lyr and nearby dwarfs with observed RR Lyr
 1389 indicate a modification between 0.048 and 0.085. From
 1390 Soltis et al. (2021), there is the single direct TRGB mea-
 1391 surement giving the modification 0.08. In no individual
 1392 case is the justification for a modification compelling,
 1393 yet the hints are strong. Gaia DR3 observations are ex-
 1394 pected to provide clarity. Under the circumstances and
 1395 as a provisional solution, we will force agreement of our
 1396 TRGB measurement for the galaxy NGC 4258 (Anand
 1397 et al. 2022) to match the maser distance to that galaxy
 1398 (Reid et al. 2019) rounded to the nearest 100th of a
 1399 magnitude, a zero point shift to smaller distances with
 1400 respect to Rizzi et al. (2007) of 0.05 mag. The weakly
 1401 color dependent TRGB calibration becomes

$$M_{I,trgb} = -4.00 + 0.22[(V - I) - 1.6] \quad (7)$$

1402 The uncertainty in the lead coefficient is dominated by
 1403 systematics between Hipparcos and Gaia parallaxes that
 1404 remain to be resolved, but an estimate ± 0.03 brackets
 1405 the range of shifts discussed above. The color term is
 1406 also subject to review. As opposed to the linear ramp
 1407 with color incorporated in Eq.7, published alternatives
 1408 are a constancy with color on the premise that the mea-
 1409 surement is made of the most metal poor of TRGB stars
 1410 (Freedman et al. 2019) or a curved refinement of our lin-
 1411 ear relation (Jang & Lee 2017).

1412 Direct comparisons can be made between CPLR dis-
 1413 tance moduli and TRGB moduli with the revised zero
 1414 point calibration using Gaia information. In the case
 1415 of eight galaxies (including NGC 4258) with TRGB es-
 1416 timates (Anand et al. 2021) and CPLR estimates from the
 1417 SH0ES collaboration (Riess et al. 2022) there is the av-
 1418 erage difference in distance modulus $<\mu_{trgb} - \mu_{cplr}> =$
 1419 0.028 ± 0.038 with rms scatter ± 0.107 . There are 10

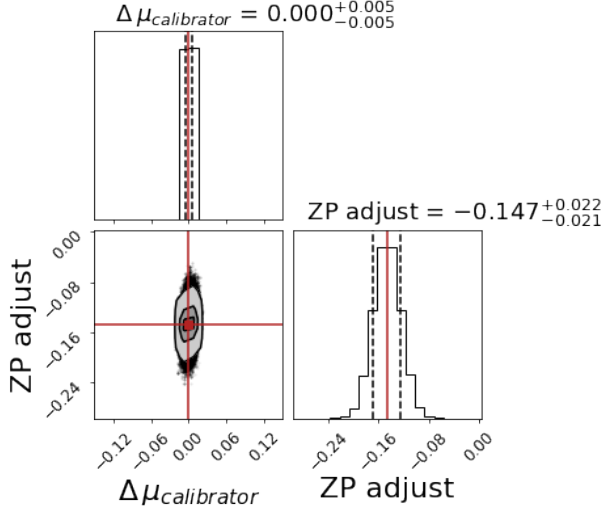


Figure 17. The posterior distribution of the zero point adjustment. Each panel covers ± 0.15 mag about the center of distribution. Other details are as in Figure 3.

galaxies in common between the TRGB distances of Anand et al. (2021) and CPLR distances of Freedman et al. (2001) (assuming LMC is at $\mu_{LMC} = 18.477$). In two cases (M66 and NGC 5253) the CPLR moduli are greater than TRGB by ~ 0.2 mag. It can be seen by eye with the TRGB fits displayed in the Extragalactic Distance Database (Anand et al. 2021) that a deviation this large is not supported by the TRGB measurements. Considering the other eight cases, there is the average difference in modulus of $\langle \mu_{trgb} - \mu_{cplr} \rangle = 0.019 \pm 0.025$ with rms scatter ± 0.069 . Combining the Riess et al. (2022) and Freedman et al. (2001) CPLR results, giving 16 comparisons, we find $\langle \mu_{trgb} - \mu_{cplr} \rangle = 0.023 \pm 0.022$ with rms scatter ± 0.087 . There is agreement between the TRGB and CPLR observations in common to within 1% with an rms scatter including errors in both inputs of 4%.

Going forward, then, our cumulative sample of zero point calibrators will consist of 489 galaxies with TRGB distance estimates (Anand et al. 2021) shifted closer by 0.05 mag in the modulus, 76 galaxies with CPLR distances on the scale of Riess et al. (2022), and 6 maser distances (Pesce et al. 2020) including the important case of NGC 4258 (Reid et al. 2019). Accounting for overlaps, 489 zero point calibrator galaxies are involved. In the union of all methodologies, the distance moduli of these calibrators in the ensemble will not shift.

The absolute distance scale calibration is established by evaluating linkages between individual calibrators and targets within the five methods ensemble discussed in §10.1. We find 128 individual galaxies among the TRGB, CPLR, maser calibrators with matches in the

combined FP, TF, SBF, SNIa, SNII samples. After rejection of three outliers (PGCs 5896, 44982, and 68535) and four Local Group galaxies, the remaining 121 matches are linked through an MCMC chain as summarized in the corner plot of Figure 17. It follows that the arbitrary 5 source scale that was set with SNIa requires the revision

$$\mu_{zp} = \mu_{5so} - 0.147 \pm 0.022 \text{ mag.} \quad (8)$$

There is significant variation in the coefficient of the revision if the five sources of inputs are considered separately. Individually (with respect to the scale of Fig. 13) $\mu_{zp} - \mu_{xxx}$ equals -0.103 ± 0.057 (TF: 81 cases), -0.052 ± 0.021 (SNIa: 44 cases), -0.208 ± 0.061 (SBF: 29 cases), and -0.152 ± 0.119 (SNII: 8 cases). There are only 3 overlaps with FP. The result with SNIa alone is anomalous. The anomaly is reduced somewhat in a comparison between groups containing calibrators and SNIa: offset -0.067 ± 0.021 mag with 49 SNIa. The difference from the 5 source value given in Eq. 8 would have a 3.7% effect on the Hubble Constant ($\Delta H_0 = -2.8 \text{ km s}^{-1} \text{ Mpc}^{-1}$). This difference in the establishment of an absolute scale calibration between referencing to SNIa alone vs. the coupling of SNIa to other methodologies is essentially identical to that found in the construction of *Cosmicflows-3* (Tully et al. 2016), see the discussion involving Fig. 12 in that paper. Going forward, we retain the more robust zero point scaling given by Eq. 8 but we recognize the plausibility of systematic errors at least as large as the ambiguity raised by the SNIa anomaly

10.3. Systematic Errors and the Path Forward

Our results support the contention that the apparent differences in the cosmic expansion velocity today between direct measurements of distances and velocities and expectations of the standard Λ CDM model from conditions in the early universe are real, but the case is not yet compelling. In our analysis the numbers of measurements are large so statistical uncertainties are very small. However the possibilities of systematic errors are a concern.

Issues can be separated between the establishment of the absolute distance scale from local observations and possible systematics in measurements well beyond the calibrators. Consider first the local problem. There is the expectation that, within a year or two, precision parallaxes provided by the Gaia experiment will provide precise intrinsic luminosities for the kinds of stars important for distance work: cepheids, RR Lyrae and horizontal branch stars, and stars at the tip of the red giant branch. The samples should be numerous enough

to unravel metallicity and age effects. Present uncertainties in the absolute scaling is at the level of several percent. Surely it is not at the 10% level required to reconcile the Hubble Constant controversy. In any event, we can expect that this problem will soon be resolved at the 1% level.

Presently the FP and TF methodologies provide the large samples required for depth and wide field coverage of the sky. However with only 20% – 25% accuracy per target, uncertainties at redshifts $0.05c - 0.1c$ are $3000 - 7500 \text{ km s}^{-1}$. Systematics that can arise from selection biases at the level of only a few percent can have several hundred km s^{-1} effects. If a sample is free of systematics it should pass our tests of Hubble parameter constancy with redshift or other parameters, but such tests are not a guarantee against problems.

Going forward, prospects for building a large all-sky sample at substantial redshifts look best with SNIa. Surveillance at high cadence with moderate aperture telescopes suffice to detect the $\sim 10^3$ SNIa within $z=0.1$ that erupt each year. With samples of many thousand, with photometry at multiple passbands and accompanying spectra, it should be possible to empirically calibrate variations in the properties of the explosion events, providing relative distances accurate to 5%. Vulnerability to systematics should be reduced roughly linearly with the improved statistical accuracy.

What remains is the coupling between the near field calibration and the far field mapping. The approach of coupling between cepheids and SNIa may be reaching its limits. Proximate SNIa are few and the requisite monitoring required to characterize distant cepheids will challenge resources. Prospects are better with TRGB, bright in the infrared and accessible to 40 Mpc or more with a single exposure sequence per target with James Webb Space Telescope (JWST). TRGB targets will couple equally to SNIa and SBF hosts. JWST will facilitate the SBF methodology with 5% distance accuracy out to $z \sim 0.07$. An all Pop II TRGB–SBF path to galaxy distances will complement the Pop I CPLR–SNIa path and the availability of two independent methodologies covering the same distance range will provide a good test of systematics.

11. SUMMARY OF THE DISTANCE INPUTS

Table 1 gathers together statistics and references pertaining to all the methodologies and all the sub-samples contributing to the study.

12. THE COSMICFLOWS-4 CATALOG

The *Cosmicflows-4* compendium of galaxy distances is presented in three tables, with a representative stub of

the first several lines of each given in the Appendix and the full tables available on line and at the *Extragalactic Distance Database* (<https://edd.ifa.hawaii.edu>).

The line entries in Table 2 give information on 55,877 individual galaxies with information pertaining to their distances. Individual distance moduli and uncertainties are given, where available, for each of the methodologies, SNIa, TF, FP, SBF, SNII, TRGB, CPLR, MASER, and a weighted average value, all on the absolute scaling established by the combined TRGB, CPLR, and MASER calibrators. The table also provides coordinates, velocities in the CMB reference frame, and Tully (2015b) and Tempel et al. (2017) group affiliations.

Table 3 gives related information for 38,065 groups. By order of preference, the group constructions draw upon the groups of Kourkchi & Tully (2017), Tully (2015b), and Tempel et al. (2017) in that order. If a galaxy is not within the samples of those groups, it can receive a group linkage through position and velocity coincidence with the virial properties of an established group. For each group with a distance estimate, the number and averaged values within each methodology are given as well as an overall averaged distance modulus value, on the absolute scale established by the TRGB, CPLR, and MASER calibrators. In the stub of this table in the Appendix, the groups are sorted by the number of group targets available with the FP methodology.

Table 4 gives derivative information for the same 38,065 groups, including coordinates, velocities in different reference frames, peculiar velocities following from Eqs. 9–11 discussed in the next section, and values of the Hubble parameter $H_i = f_i V_{cmb,i} / d_i$ for each group.

13. PROPERTIES OF THE CATALOG

With the expectation that peculiar velocities are of order 300 km s^{-1} , beyond about $4,000 \text{ km s}^{-1}$ it is anticipated that motions due to cosmological expansion will dominate. Accordingly, a necessary but not sufficient test our distance measures should pass is rough constancy in the value of the Hubble parameters with redshift after exclusion of the nearby realm. Our collection of distances pass this test as seen in Figure 18. Here, each gray dot is at the Hubble parameter and velocity location of a group, including groups of one. Heavier blue dots identify groups with uncertainties 5% or better in distance. The overall average for groups at greater than $4,000 \text{ km s}^{-1}$ is $\log H_0 = 1.875$ corresponding to $H_0 = 75.0 \text{ km s}^{-1} \text{ Mpc}^{-1}$. The logarithmic rms scatter is ± 0.092 . The statistical standard deviation on H_0 with 35,004 groups is only $\pm 0.2 \text{ km s}^{-1} \text{ Mpc}^{-1}$, smaller than the uncertainty in the zero point calibration through Eq. 8 of $\pm 0.8 \text{ km s}^{-1} \text{ Mpc}^{-1}$.

Table 1. Summary of all distance contributions

Method	Sub-Sample	Number of Distances	Reference
TF	12223 galaxies in 10188 groups		
	cf4	9323	Kourkchi et al. (2022)
	spitzer	2202	Sorce et al. (2014)
	cf2	4014	Tully et al. (2013)
	sfi	3938	Springob et al. (2007)
	2mtf	1712	Hong et al. (2019)
	flat	546	Makarov et al. (2018)
FP	42223 galaxies in 27691 groups		
	sdss	34045	Howlett et al. (2022)
	6dfgsv	7099	Qin et al. (2018)
	smac	689	Hudson et al. (2001)
	enear	447	Bernardi et al. (2002)
	efar	696	Colless et al. (2001)
SBF	480 galaxies in 227 groups		
	vir/for	134	Blakeslee et al. (2010)
	tonry	297	Tonry et al. (2001)
	cantiello	89	Cantiello et al. (2018a)
	ir/hst	63	Jensen et al. (2021)
SNIa	1008 galaxies in 945 groups		
	sh0es	560	Riess et al. (2022)
	pantheonplus	589	Scolnic et al. (2021)
	scolnic	514	Early Pantheon compilation
	csp1	137	Burns et al. (2018)
	loss	235	Ganeshalingam et al. (2013)
	rest	198	Rest et al. (2014)
	union2	248	Amanullah et al. (2010)
	jha	119	Jha et al. (2007)
	prieto	87	Prieto et al. (2006)
	constitution	205	Hicken et al. (2009)
	folatelli	28	Folatelli et al. (2010)
	walker	29	Walker et al. (2015)
	stahl	669	Stahl et al. (2021)
	twins	133	Boone et al. (2021)
	avelino	89	Avelino et al. (2019)
SNII	94 galaxies in 94 groups		
	de Jaeger	94	de Jaeger et al. (2020b)
TRGB	489 galaxies		
	edd	489	Anand et al. (2021)
CPLR	76 galaxies		
	riess	40	Riess et al. (2022)
	keyproject	23	Freedman et al. (2001)
	nearby	12	Bhardwaj et al. (2016)
	bentz	1	Bentz et al. (2019)
MASER	6 galaxies		
	pesce	5	Pesce et al. (2020)
	ngc4258	1	Reid et al. (2019)

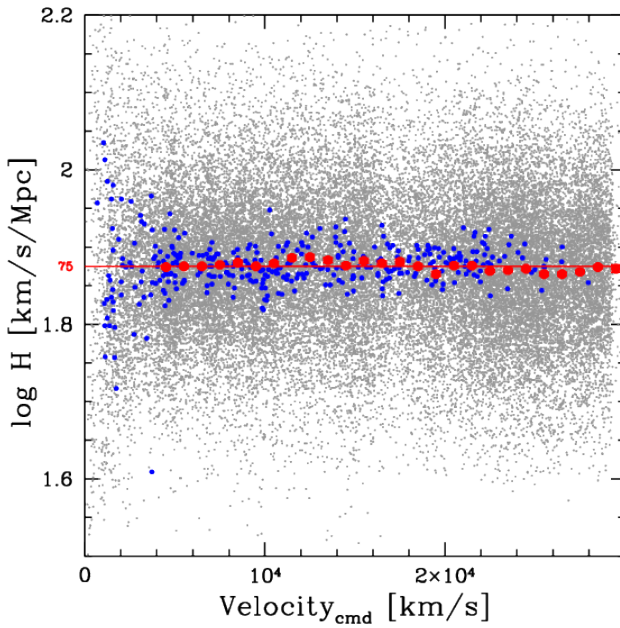


Figure 18. Hubble parameter vs. systemic velocity. Individual groups are identified in gray while groups with uncertainties in modulus 0.10 mag or better are highlighted in blue. Red symbols with (small) error bars denote mean $\log H$ values in 1000 km s^{-1} intervals. The overall average of values for $V > 4000 \text{ km s}^{-1}$ is given by the horizontal red line.

Contributions to our collection of distances have distinct sky coverage. There is the risk of offsets between contributions that would result in artificial flows between regions dominated by different inputs. Our Bayesian linkages between methods minimize such problems. The expectation is that there would not be suspicious trends between sectors of the sky dominated by different sources. The three numerically largest contributions come from the two FP programs; SDSS and 6dFGSv that are restricted to the northern and southern sky respectively and the TF programs that have emphasis in northern sky coverage. The displays in Figure 19 break down the all-sky coverage of Figure 18 into four sectors, whether north or south on the celestial sky and whether north or south of the galactic plane. The sky coverage is obviously uneven. The only abundant coverage beyond $16,000 \text{ km s}^{-1}$ is in the sector north celestial and north galactic, as provided by SDSS FP. A sprinkle of coverage at high velocities is provided by SNIa contributions. Trends can be detected between sectors, most notably elevated Hubble values in the south celestial – north galactic sector and slightly depressed Hubble values in the opposite north celestial – south galactic sector. This pattern can be attributed to the known motion toward the so-called Great Attractor (Dressler

et al. 1987a) and the kinematic response associated with the cosmic microwave background temperature dipole (Fixsen et al. 1996).

The observed radial motions of galaxies derive from a combination of the expansion of the universe and deviations assumed to arise from gravitational perturbations. This latter component, commonly called the peculiar velocity, can be extracted with knowledge of the distance of the system and of the mean expansion of the universe characterized by Hubble's constant, following Davis & Scrimgeour (2014)

$$V_{\text{pec}}^{\text{ds}} = (fV_{\text{cmb}} - H_0 d) / (1 + H_0 d/c). \quad (9)$$

The cosmological curvature correction parameter f was defined in connection with Eq. 3. As is well known, uncertainties in peculiar velocities skew to larger negative values in the translation from logarithmic distance modulus to distance. A formulation to negate the skewness and dampen the amplitude of peculiar velocities in the presence of uncertainties was developed by Watkins & Feldman (2015)

$$V_{\text{pec}}^{\text{wf}} = \frac{fV_{\text{cmb}}}{1 + fV_{\text{cmb}}/c} \log(fV_{\text{cmb}}/H_0 d). \quad (10)$$

This approximation has application if $v_{\text{pec}} \ll H_0 d$. For present rough purposes, we estimate peculiar velocities with Eq. 9 nearby where peculiar velocities can be a substantial fraction of observed velocities, transitioning to Eq. 10 by velocity $V_{ls} = 3000 \text{ km s}^{-1}$ in the Local Sheet frame (Tully et al. 2008), with the ramp

$$V_{\text{pec}} = V_{\text{pec}}^{\text{ds}}(1 - V_{ls}/3000) + V_{\text{pec}}^{\text{wf}}V_{ls}/3000. \quad (11)$$

A histogram of the peculiar velocities of all of the 38,000 groups, all those represented in gray in Figure 18, is seen in the top panel of Figure 20, while the bottom panel zooms to the histogram for groups with distance modulus uncertainties 0.10 mag or better, the blue points in Figure 18. The distribution of peculiar velocities with well constrained distances is approximated by a Gaussian distribution with standard deviation 300 km s^{-1} .

13.1. A preliminary look at sky coverage

The distribution of all the entities in the group catalog are shown in the two orthogonal projections of Figure 21. The coverage is dense and relatively uniform around the sky within $\sim 8,000 \text{ km s}^{-1}$ except for the Milky Way avoidance zone at $SGY \sim 0$. The two FP samples provide coverage in two distinct fans: 6dFGSv out to $16,000 \text{ km s}^{-1}$ in the celestial south and SDSS out to $30,000 \text{ km s}^{-1}$ in the north galactic and celestial polar cap. There is only spotty coverage in the sector in the

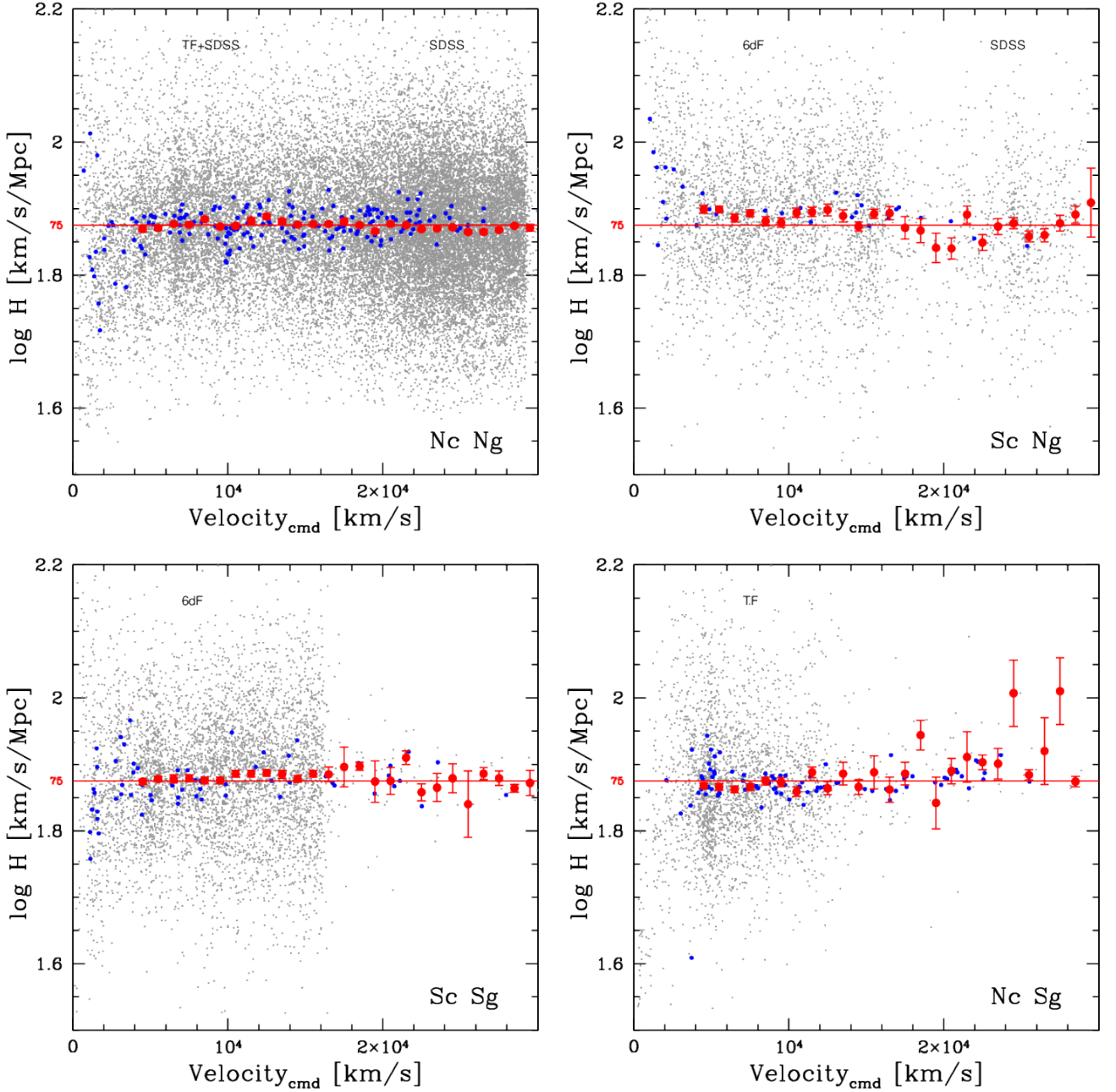


Figure 19. Hubble parameter vs. systemic velocity separated into four sectors: north (N) and south (S) celestial (c) and galactic (g) quadrants. Gray, blue and red symbols are the same as in Fig. 18. Dominant contributing methodologies in each of the sectors are specified across the top of panels: SDSS FP restricted to the north celestial and galactic cap, 6dFGSv FP restricted to the celestial south, TF everywhere across the sky but favoring the declination range accessed by Arecibo Telescope, and other methods widely distributed but relatively sparse. The means in $\log H$ are noisy at $V > 16,000 \text{ km s}^{-1}$ in sectors where the contributions come mostly from a few SNIa. $\log H$ values tend to lie above the mean line in the ScNg sector, in the direction toward the apex of the cosmic microwave background dipole, and tend to lie below the mean line in the anti-apex NcSg quadrant.

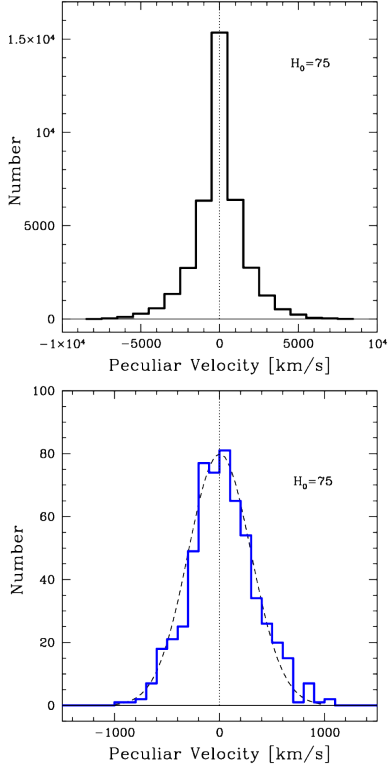


Figure 20. Top: Histogram of 38,065 group peculiar velocities. Bottom: Histogram of peculiar velocities for 581 groups with distance uncertainties better than 5%. The dashed curve illustrates a Gaussian distribution with standard deviation 300 km s^{-1} .

northern sky south of the Galaxy at velocities greater than $8,000 \text{ km s}^{-1}$ where the range of TF coverage falls off (see the histogram of Fig. 1).

The most dramatic feature seen in these projections contains as a component the Sloan Great Wall (Vogeley et al. 2004; Gott et al. 2005) at $SGY \sim 20,000 \text{ km s}^{-1}$. The Center for Astrophysics Great Wall (de Lapparent et al. 1986) is seen a $SGY \sim 6,000 \text{ km s}^{-1}$.

While there is vast terrain to explore opened up by the full SDSS FP sample, uncertainties in individual distance measurements are extreme in the outer regions, and there will continue to be particular interest in the volume of reasonably uniform coverage. As is seen in Figure 22, the ensemble sample is reasonably dispersed within $16,000 \text{ km s}^{-1}$ except for the fall-off beyond $\sim 8000 \text{ km s}^{-1}$ in the celestial north outside the boundaries of the SDSS study, at positive SGX and positive SGZ. There is the usual caveat regarding the zone of obscuration.

Figures 23 and 24 expand views to the inner $8,000 \text{ km s}^{-1}$ volume where the TF coverage is of principal importance and individual peculiar velocities are tractable. Fig. 24 shows $5,000 \text{ km s}^{-1}$ slices in SGY on

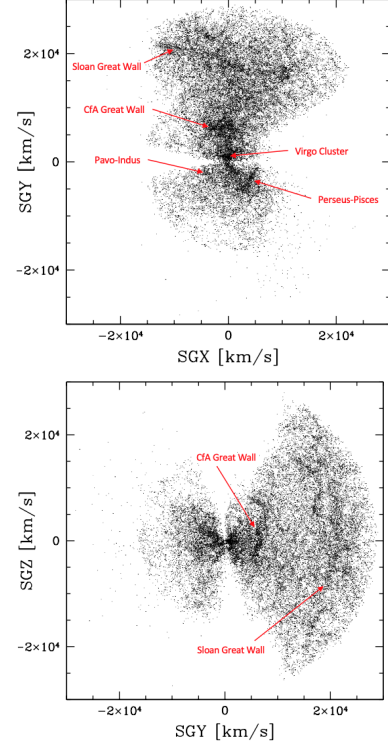


Figure 21. Two views of the ensemble of groups in supergalactic coordinates. The obscuration zone of the Milky Way lies slightly tilted at $SGY \sim 0$. The extensive SDSS FP sample in the north galactic, north celestial sector is evident at $SGY > 0$. Both the Sloan and CfA Great Walls are evident. A sprinkle of points representing SNIa hosts can be seen within the domain extending to $z = 0.1$.

the north and south sides of the galactic plane in the direction orthogonal to the views of Figs. 21–23. The complex networks of filaments await detailed morphological and dynamic studies.

14. SUMMARY

Cosmicflows-4 combines distances from eight methodologies: five reaching galaxies over a substantial volume and three providing anchors of the absolute scale. The case for a controlled homogeneous approach to establishing distances is well founded (Riess et al. 2019), but the use of a heterogeneous sample also has merits. The possibility of systematic errors is now more worrisome than statistical errors. The exploration of multiple paths can reveal differences that warn of the occurrence of systematics.

The various methodologies are meshed together by overlaps. The only substantial overlaps between individual galaxies within *Cosmicflows-4* involve a moderate number of matches with SNIa events. More robust linkages are through common memberships in groups. Here, three group catalogs are employed, by order of priority

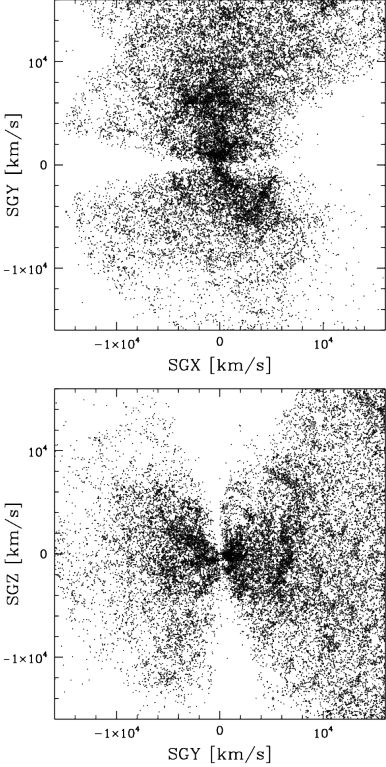


Figure 22. Zoom in on the two panels of Fig. 21. Within $16,000 \text{ km s}^{-1}$ there is reasonable sky coverage except at large positive SGX and the zone of obscuration. An [interactive 3D visualization](#) of the distribution of groups provides further insights.

those by Kourkchi & Tully (2017), Tully (2015b), and Tempel et al. (2017). The importance of the group linkages should not be underestimated. In the extreme, in each of the clusters Coma and Hercules there are ~ 200 FP measures and 50–60 TF measures. The two clusters have hosted 9 of our SNIa.

Our absolute scaling also comes through groups affiliations, those involving galaxies with TRGB, CPLR, or maser distances. With this step, as with all the precursor steps involving the integration of individual methodologies and the uniting of methodologies, the merging was carried out with a Markov Chain Monte-Carlo sampling from probability distributions governed by error assignments.

Our best value for the Hubble constant of $H_0 = 75.0 \text{ km s}^{-1} \text{ Mpc}^{-1}$ has a formal statistical error of only $\pm 0.8 \text{ km s}^{-1} \text{ Mpc}^{-1}$. However as discussed in §10.2, the calibration is lowered by $2.8 \text{ km s}^{-1} \text{ Mpc}^{-1}$ if the only coupling is through SNIa. Let us try to be clear on the separate routes to H_0 giving these different results. With our preferred route, the 1008 SNIa are merged with the FP, TF, SBF, and SNII material onto a common but arbitrary scale, then this ensemble is merged

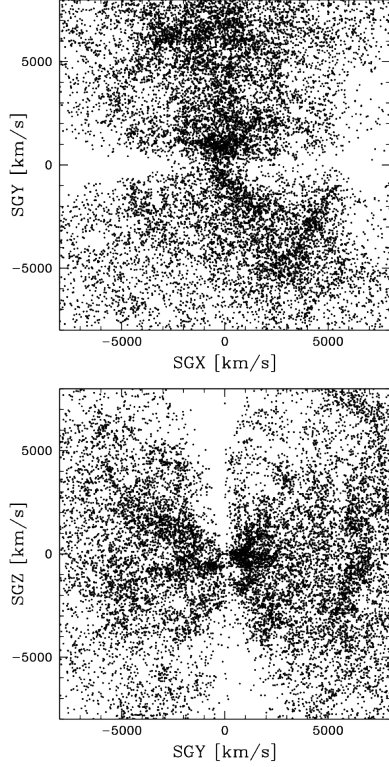


Figure 23. A further zoom in on the two panels of Figs. 21 and 22. Outside the zone of obscuration there is reasonably uniform coverage with sky direction within this domain.

with 128 galaxies involving some combination of the TRGB, CPLR, and maser calibrators. In the alternate route, the linkage involves establishing the SNIa scale alone with 44 SNIa host galaxies with TRGB, CPLR, or maser information. This latter route giving $H_0 = 72.2 \text{ km s}^{-1} \text{ Mpc}^{-1}$ is in good agreement with the value by Riess et al. (2022) of $H_0 = 73.0 \pm 1.0 \text{ km s}^{-1} \text{ Mpc}^{-1}$ involving much the same input. The same systematic difference was found between an ensemble of methodologies approach versus SNIa only in the compilation of *Cosmicflows-3* (Tully et al. 2016).

Is the difference due to modest number statistics? Or could the difference arise because SNIa involved in the zero point calibration are systematically different from the ensemble of observed SNIa? The absolute values of SNIa are suspected to vary with host properties, possibly related to the mean ages of explosions (Hayden et al. 2013; Childress et al. 2013; Roman et al. 2018). We are warned that systematics at the level of 3% in the absolute scale are possible, not including the grounding by geometric parallaxes that Gaia DR3 should illuminate.

In any event, the primary motivation for the *Cosmicflows* program is the study of *deviations* from cosmic expansion which are independent of the absolute scale calibration. Our goal is to compile a catalog of dis-

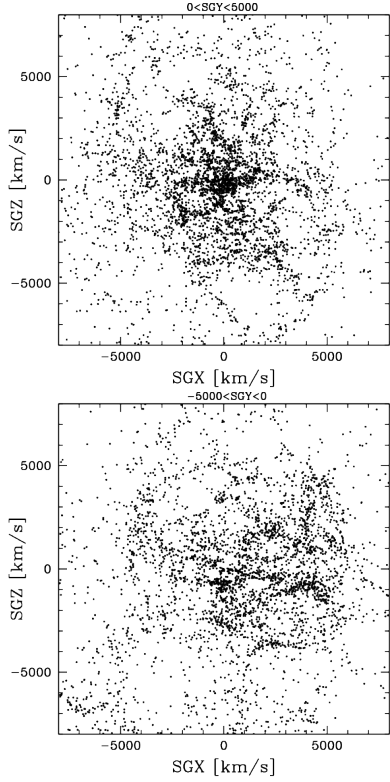


Figure 24. The view almost normal to the galactic plane restricted to $\pm 5000 \text{ km s}^{-1}$ and separating between north of the Galaxy (top panel) and the galactic south (bottom).

tances that, although they have uncertainties, are unbiased in relative distances. There is no recourse to information about the distribution of mass through redshift surveys or other considerations. It is well known that biases can arise in the inference of peculiar velocities from distances with large errors beyond what is captured by Eq. 10. Mitigating efforts with past samples of galaxy distances involve Wiener filtering or Bayesian coupling with the inferred distribution of mass from redshift catalogs (Courtois et al. 2012; Hoffman et al. 2015, 2021; Carrick et al. 2015; Jasche & Lavaux 2019; Graziani et al. 2019; Lilow & Nusser 2021). It is expected that the availability of the present catalog of distances will lead to even more extensive studies.

There are deficiencies with the present catalog where improvements can be realized. It is anticipated that the absolute scale foundation given by geometric parallaxes will soon be established more rigorously with the release of Gaia DR3. Throughout, there is a need for greater overlaps between methodologies. SNIa will continue to play an important role, with the possibility of accumulating samples of many thousands in the near future. It will be difficult to seriously expand the CPLR samples with current space facilities. However the alternate

Population II route of TRGB linked to SBF should be a profitable way forward with James Webb Space Telescope. There is the prospect of acquiring considerably larger samples than with CPLR–SNIa with comparable accuracy per target. The availability of a second independent path will be a real test of systematics.

15. ACKNOWLEDGEMENTS

We thank an anonymous referee for a gracious review. Funding over the many years of the *Cosmicflows* project has been provided by the US National Science Foundation grant AST09-08846, the National Aeronautics and Space Administration grant NNX12AE70G, and multiple awards to support observations with Hubble Space Telescope through the Space Telescope Science Institute. The resources of the NASA-IPAC Extragalactic Database and HyperLEDA hosted in Lyon, France have been indispensable. B.E.S. was supported by the Marc J. Staley graduate fellowship at UC Berkeley.

DATA AVAILABILITY

We presented all data underlying this article in three Appendix tables. The complete versions of these tables are available within the public domain of the Extragalactic Distance Database (EDD: <https://edd.ifa.hawaii.edu/dfirst.php>) where Table 2 is called “All CF4 Individual Distances”, Table 3 is called “All CF4 Groups”, and Table 4 is called “CF4 All Group Velocities”.

APPENDIX

An overview of the *Cosmicflows-4* products was given in §12. The three tables provide information on (1) each individual galaxy with a distance measurement, (2) the distance properties averaged over members of groups, and (3) inferred properties from the velocities of the groups.

The information on individual galaxies in Table 2 by column:

1. PGC: The Principal Galaxies Catalog identification of the galaxy in HyperLEDA (<https://leda.univ-lyon1.fr>).
2. 1PGC: The PGC ID of the dominant galaxy in the group containing the galaxy in question given directly or inferred from the group catalogs of Kourkchi & Tully (2017) or Tully (2015b).
3. T17: The group identification given by Tempel et al. (2017).
4. V_{cmb} : Systemic velocity of the galaxy in the reference frame of the cosmic microwave background.
5. DM: Distance modulus of the galaxy derived from an MCMC analysis incorporating all methodologies and associated uncertainty.

- 1835 6–13. DM_{xxx} : Distance moduli and uncertainties of 1886
 1836 the following methodologies after registration to a com- 1887
 1837 mon scale with the MCMC analysis: (6) SNIa, (7) TF, 1888
 1838 (8) FP, (9) SBF, (10) SNII, (11) TRGB, (12) CPLR, 1889
 1839 (13) MASER.
 1840 14–19. Celestial, galactic, and supergalactic coordi-
 1841 nates of the galaxy.
- 1842 The information on groups of galaxies in Table 3 by
 1843 column:
 1844 1. 1PGC: The PGC identification of the dominant
 1845 galaxy in the group in question, given directly or inferred
 1846 from the group catalogs of Kourkchi & Tully (2017),
 1847 Tully (2015b), and Tempel et al. (2017). If from the
 1848 latter source, the 1PGC identification is associated with
 1849 the brightest galaxy in the *Cosmicflows-4* collection.
 1850 2. DM: The distance modulus and uncertainty of the
 1851 group, weighted averaged over all members of the group
 1852 with measured distance moduli.
 1853 3. V_{cmb} : Systemic velocity of group in frame of cosmic
 1854 microwave background.
 1855 4–16. Number of galaxies in group with a distance
 1856 contribution by a specific methodology and the weighted
 1857 average modulus of the specific modulus, with uncer-
 1858 tainties. Columns by methodology are (4,5) TRGB,
 1859 CPLR, or MASER calibrator, (6,7) SNIa, (8,9) FP,
 1860 (10,11) TF, (12-13) SBF from optical observations, (14-
 1861 15) SBF from infrared observations, (16) SNII (never
 1862 more than one occurrence in these groups).
- 1863 The information on velocity related information per-
 1864 taining to the groups in Table 4 by column:
 1865 1. 1PGC: The PGC identification of the dominant
 1866 galaxy in group as in Table 3, column 1.
 1867 2. DM: The same distance modulus and uncertainty
 1868 of the group averaged over all members of the group
 1869 with measured distance moduli as in Table 3, column 2.
 1870 3. d : The luminosity distance corresponding to the
 1871 modulus in column 2.
 1872 4–7. V_{xxx} : Group velocities in respectively the refer-
 1873 ence frames of the Sun, the Local Sheet (Tully et al.
 1874 2008), and the cosmic microwave background. The
 1875 value in column 7 is the value in column 6 multiplied
 1876 by the cosmological curvature adjustment parameter
 1877 $f_i = 1 + 1/2[1 - q_0]z_i - 1/6[1 - q_0 - 3q_0^2 + j_0]z_i^2$, where
 1878 z_i is the redshift of the galaxy, q_0 and j_0 are the accel-
 1879 eration and jerk parameters and c is the speed of light.
 1880 Values for the matter and vacuum energy density of the
 1881 universe $\Omega_m = 0.27$ and $\Omega_\Lambda = 0.73$ are assumed.
 1882 8–10. V_{pxx} : The peculiar velocity of the group fol-
 1883 lowing from Eqs. 9, 10, and 11 respectively. The latter
 1884 is the reference peculiar velocity of this study.
 1885 11. H_i : Group Hubble parameter, $H_i = f_i V_{cmb,i} / d_i$.

Table 2. Distances of Individual Galaxies[†]

PGC	1PGC	T17	V_{cmb} (km/s)	DM (mag)	DM_{snIa} (mag)	DM_{tf} (mag)	DM_{fp} (mag)	DM_{sbf} (mag)	DM_{snII} (mag)	DM_{trgb} (mag)	$DM_{cluster}$ (mag)	RA (deg)	DE (deg)	glat (deg)	sgl (deg)	sgb (deg)		
(1)	(2)	(3)	(4)	(5)	(6)	(7)	(8)	(9)	(10)	(11)	(12)	(13)	(14)	(15)	(16)	(17)	(18)	(19)
2	73150	0	4726	34.535±0.460	34.535±0.46							0.0070	47.2745	113.9553	-14.6992	341.6440	20.7388	
4	120	0	4109	33.495±0.390	33.495±0.39							0.0144	23.0876	107.8322	-38.2729	316.0587	18.4514	
12	12	0	6195	34.995±0.410	34.995±0.41							0.0358	-6.3739	90.1920	-65.9300	286.4249	11.3511	
16	16	0	5312	34.655±0.450	34.655±0.45							0.0471	-5.1587	91.6006	-64.8655	287.6120	11.7030	
35	35	0	34	29.730±0.100								0.0938	39.4955	112.3102	-22.3207	333.3464	20.3429	
55	55	0	4454	34.245±0.390	34.245±0.39							0.1558	33.6009	110.9496	-28.0857	327.0996	19.7763	
64	72642	0	15324	36.606±0.630								0.2180	-35.8436	350.7982	-76.1593	258.4801	1.3810	
66	72642	0	14725	36.276±0.590								0.2215	-35.9863	350.3084	-76.0782	258.3474	1.3282	
68	68	0	7338	34.735±0.560								0.2306	-18.9589	65.4189	-75.8101	274.3903	7.1770	
70	70	0	6447	35.325±0.390								0.2336	20.3380	107.1780	-40.9837	313.2487	17.7662	

[†] The complete version of this table is available online and also as the catalog "All CF4 Individual Distances" within the Extragalactic Distance Database (https://edd_ifa.hawaii.edu). The following catalogs are available pertaining to the separate methodologies: column 6 "All Cf4 SNIa Samples", column 7 "All Cf4 TFR Samples", column 8 "All Cf4 FP Samples", column 9 "All Cf4 SBF Samples" (infrared), column 10 "HST IR SBF" (optical) and "HST IR SBF" (infrared), column 11 "All Cf4 SNIT", column 12 "All Cf4 Cepheid", and column 13 "All Cf4 Maser". Distances in the catalogs for separate methodologies are on arbitrary zero point scales.

Table 3. Distances of Galaxy Groups[†]

1PGC	DM mag	V _{cmb} km/s	N _c	DM _{cal} mag	N _{sniIa}	DM _{sniIa} mag	N _{fp}	DM _{fp} mag	N _{tf}	DM _{tf} mag	N _{sbf_o}	DM _{sbf_o} mag	N _{sbf_i}	DM _{sbf_i} mag	
(1)	(2)	(3)	(4)	(5)	(6)	(7)	(8)	(9)	(10)	(11)	(12)	(13)	(14)	(15)	(16)
44715	34.891±0.025	7193	0	0.000	7	34.96±0.06	209	34.964±0.033	50	34.79±0.07	0	2	34.865±0.077		
56962	36.004±0.028	11266	0	0.000	2	36.05±0.11	193	36.065±0.035	60	35.91±0.05	0	0			
58265	35.498±0.038	9197	0	0.000	2	35.68±0.12	146	35.510±0.040	2	35.72±0.29	0	0			
36071	36.980±0.042	17476	0	0.000	1	37.02±0.18	129	37.006±0.043	0		0	0			
55151	37.373±0.046	19859	0	0.000	0		115	37.393±0.046	0		0	0			
47202	36.392±0.051	14695	0	0.000	1	36.84±0.13	93	36.391±0.064	13	36.22±0.11	0	0			
45753	37.423±0.057	21182	0	0.000	0		77	37.443±0.057	0		0	0			
51335	37.395±0.056	21561	0	0.000	0		74	37.415±0.056	0		0	0			
47982	37.220±0.056	21615	0	0.000	0		73	37.240±0.056	0		0	0			
42543	37.416±0.057	21345	0	0.000	0		71	37.436±0.057	0		0	0			
...															

[†] The complete version of this table is available online and also as the catalog "CF4 All Groups" within the Extragalactic Distance Database (<https://edd.ifa.hawaii.edu>). The following catalogs are available pertaining to the separate methodologies: column 5 "CF4 All Calibrator Groups", column 7 "CF4 SNIa Groups", column 9 "CF4 FP Groups", column 11 "CF4 TFR Groups", columns 13 and 15 "CF4 SBF Groups", column 16 "CF4 SNII Groups". Distances in the catalogs for separate methodologies are on arbitrary zero point scales.

Table 4. Galaxy Group Distances and Peculiar Velocities[†]

1PGC	DM	d	V_{hel}	V_{ls}	$V_{cm}b$	fV	V_{pds}	V_{pwf}	V_{pec}	H_i	log H	RA	DE	glon	glat	sgr	SGX	SGY	SGZ
(1)	Mpc	Mpc	km/s	km/s	km/s	km/s	km/s	km/s	km/s	(11)	(12)	deg	deg	deg	deg	deg	Mpc	Mpc	Mpc
(2)	(3)	(4)	(5)	(6)	(7)	(8)	(9)	(10)	(11)	(12)	(13)	(14)	(15)	(16)	(17)	(18)	(19)	(20)	(21)
12	34.995±0.410	99.8	6532	6669	6179	6280	-1174	-468	62.9	1.799	0.0360	-6.3739	90.1922	-65.9300	286.4249	11.3510	1848	-6271	1312
14	36.095±0.380	165.6	11837	12035	11474	11820	-575	-244	71.4	1.854	359.9805	8.1846	101.6600	-52.5465	300.8070	15.3909	5942	-9967	3194
16	34.655±0.450	85.3	5709	5851	5354	5430	-948	-380	63.6	1.804	0.0470	-5.1587	91.6006	-64.8655	287.6120	11.7030	1733	-5461	1187
35	29.730±0.100	8.8	335	618	28	28	-633	-38	3.2	0.501	0.0938	39.4955	112.3102	-22.3207	333.3464	20.3429	518	-260	215
55	34.245±0.390	70.6	4791	5064	4466	4519	-765	-307	64.0	1.806	0.1558	33.6010	110.9495	-28.0857	327.0996	19.7763	4001	-2589	1713
63	35.245±0.410	111.9	8743	9004	8404	8590	189	83	76.7	1.885	359.9338	28.2883	109.3762	-33.2252	321.4869	19.2652	6651	-5294	2971
68	34.735±0.560	88.5	7684	7759	7358	7501	844	388	84.7	1.928	0.2305	-18.9590	65.4189	-75.8101	274.3903	7.1770	589	-7676	969
70	35.325±0.390	116.1	6803	7043	6450	6560	-2090	-791	56.5	1.752	0.2334	20.3381	107.1779	-40.9836	313.2488	17.7663	4555	-4886	2149
75	36.384±0.345	189.1	11750	11700	11521	11870	-2212	-884	62.8	1.798	0.3388	-43.6117	331.2258	-70.6612	251.2392	-1.4353	-3762	-11074	-293
76	34.885±0.390	94.8	6903	7166	6566	6680	-423	-178	70.4	1.848	0.2454	28.9118	109.8059	-32.6706	322.1729	19.1316	5347	-4152	2348
...																			

[†] The complete version of this table is available online and also as the catalog "CF4 All Group Velocities" within the Extragalactic Distance Database (<https://edd.ifa.hawaii.edu>).

REFERENCES

- 1891 Abolfathi, B., Aguado, D. S., Aguilar, G., et al. 2018,
 1892 ApJS, 235, 42, doi: [10.3847/1538-4365/aa9e8a](https://doi.org/10.3847/1538-4365/aa9e8a)
- 1893 Adhikari, S., Dalal, N., & Chamberlain, R. T. 2014, JCAP,
 1894 2014, 019, doi: [10.1088/1475-7516/2014/11/019](https://doi.org/10.1088/1475-7516/2014/11/019)
- 1895 Alam, S., Albareti, F. D., Allende Prieto, C., et al. 2015,
 1896 ApJS, 219, 12, doi: [10.1088/0067-0049/219/1/12](https://doi.org/10.1088/0067-0049/219/1/12)
- 1897 Amanullah, R., Lidman, C., Rubin, D., et al. 2010, ApJ,
 1898 716, 712, doi: [10.1088/0004-637X/716/1/712](https://doi.org/10.1088/0004-637X/716/1/712)
- 1899 Anand, G. S., Tully, R. B., Rizzi, L., Riess, A. G., & Yuan,
 1900 W. 2022, ApJ, 932, 15, doi: [10.3847/1538-4357/ac68df](https://doi.org/10.3847/1538-4357/ac68df)
- 1901 Anand, G. S., Tully, R. B., Rizzi, L., Shaya, E. J., &
 1902 Karachentsev, I. D. 2019, ApJ, 880, 52,
 1903 doi: [10.3847/1538-4357/ab24e5](https://doi.org/10.3847/1538-4357/ab24e5)
- 1904 Anand, G. S., Rizzi, L., Tully, R. B., et al. 2021, AJ, 162,
 1905 80, doi: [10.3847/1538-3881/ac0440](https://doi.org/10.3847/1538-3881/ac0440)
- 1906 Avelino, A., Friedman, A. S., Mandel, K. S., et al. 2019,
 1907 ApJ, 887, 106, doi: [10.3847/1538-4357/ab2a16](https://doi.org/10.3847/1538-4357/ab2a16)
- 1908 Bartier, C.-L., Jensen, J., & Blakeslee, J. 2017, in American
 1909 Astronomical Society Meeting Abstracts, Vol. 229,
 1910 American Astronomical Society Meeting Abstracts #229,
 1911 143.05
- 1912 Beaton, R. L., Bono, G., Braga, V. F., et al. 2018, SSRv,
 1913 214, 113, doi: [10.1007/s11214-018-0542-1](https://doi.org/10.1007/s11214-018-0542-1)
- 1914 Benedict, G. F., McArthur, B. E., Feast, M. W., et al.
 1915 2007, AJ, 133, 1810, doi: [10.1086/511980](https://doi.org/10.1086/511980)
- 1916 Bentz, M. C., Ferrarese, L., Onken, C. A., Peterson, B. M.,
 1917 & Valluri, M. 2019, ApJ, 885, 161,
 1918 doi: [10.3847/1538-4357/ab48fb](https://doi.org/10.3847/1538-4357/ab48fb)
- 1919 Bernardi, M., Alonso, M. V., da Costa, L. N., et al. 2002,
 1920 AJ, 123, 2990, doi: [10.1086/340463](https://doi.org/10.1086/340463)
- 1921 Bhardwaj, A., Kanbur, S. M., Macri, L. M., et al. 2016, AJ,
 1922 151, 88, doi: [10.3847/0004-6256/151/4/88](https://doi.org/10.3847/0004-6256/151/4/88)
- 1923 Blakeslee, J. P., Jensen, J. B., Ma, C.-P., Milne, P. A., &
 1924 Greene, J. E. 2021, ApJ, 911, 65,
 1925 doi: [10.3847/1538-4357/abe86a](https://doi.org/10.3847/1538-4357/abe86a)
- 1926 Blakeslee, J. P., Jordán, A., Mei, S., et al. 2009, ApJ, 694,
 1927 556, doi: [10.1088/0004-637X/694/1/556](https://doi.org/10.1088/0004-637X/694/1/556)
- 1928 Blakeslee, J. P., Cantiello, M., Mei, S., et al. 2010, ApJ,
 1929 724, 657, doi: [10.1088/0004-637X/724/1/657](https://doi.org/10.1088/0004-637X/724/1/657)
- 1930 Boone, K., Aldering, G., Antilogus, P., et al. 2021, ApJ,
 1931 912, 71, doi: [10.3847/1538-4357/abec3b](https://doi.org/10.3847/1538-4357/abec3b)
- 1932 Brout, D., Taylor, G., Scolnic, D., et al. 2021, arXiv
 1933 e-prints, arXiv:2112.03864.
<https://arxiv.org/abs/2112.03864>
- 1935 Burns, C. R., Parent, E., Phillips, M. M., et al. 2018, ApJ,
 1936 869, 56, doi: [10.3847/1538-4357/aae51c](https://doi.org/10.3847/1538-4357/aae51c)
- 1937 Campbell, L. A., Lucey, J. R., Colless, M., et al. 2014,
 1938 MNRAS, 443, 1231, doi: [10.1093/mnras/stu1198](https://doi.org/10.1093/mnras/stu1198)
- 1939 Cantiello, M., Blakeslee, J. P., Ferrarese, L., et al. 2018a,
 1940 ApJ, 856, 126, doi: [10.3847/1538-4357/aab043](https://doi.org/10.3847/1538-4357/aab043)
- 1941 Cantiello, M., Jensen, J. B., Blakeslee, J. P., et al. 2018b,
 1942 ApJL, 854, L31, doi: [10.3847/2041-8213/aaad64](https://doi.org/10.3847/2041-8213/aaad64)
- 1943 Carretta, E., Gratton, R. G., Clementini, G., & Fusi Pecci,
 1944 F. 2000, ApJ, 533, 215, doi: [10.1086/308629](https://doi.org/10.1086/308629)
- 1945 Carrick, J., Turnbull, S. J., Lavaux, G., & Hudson, M. J.
 1946 2015, MNRAS, 450, 317, doi: [10.1093/mnras/stv547](https://doi.org/10.1093/mnras/stv547)
- 1947 Childress, M., Aldering, G., Antilogus, P., et al. 2013, ApJ,
 1948 770, 108, doi: [10.1088/0004-637X/770/2/108](https://doi.org/10.1088/0004-637X/770/2/108)
- 1949 Cho, H., Blakeslee, J. P., Chies-Santos, A. L., et al. 2016,
 1950 ApJ, 822, 95, doi: [10.3847/0004-637X/822/2/95](https://doi.org/10.3847/0004-637X/822/2/95)
- 1951 Clementini, G., Garofalo, A., Muraveva, T., & Ripepi, V.
 1952 2018, in Astronomical Society of the Pacific Conference
 1953 Series, Vol. 514, Stellar Populations and the Distance
 1954 Scale, ed. J. Jensen, R. M. Rich, & R. de Grijs, 89.
<https://arxiv.org/abs/1804.09575>
- 1955 Colless, M., Saglia, R. P., Burstein, D., et al. 2001,
 1956 MNRAS, 321, 277
- 1957 Courtois, H. M., Hoffman, Y., Tully, R. B., & Gottlöber, S.
 1958 2012, ApJ, 744, 43, doi: [10.1088/0004-637X/744/1/43](https://doi.org/10.1088/0004-637X/744/1/43)
- 1959 Courtois, H. M., Tully, R. B., Fisher, J. R., et al. 2009, AJ,
 1960 138, 1938, doi: [10.1088/0004-6256/138/6/1938](https://doi.org/10.1088/0004-6256/138/6/1938)
- 1961 Courtois, H. M., Tully, R. B., & Héraudeau, P. 2011a,
 1962 MNRAS, 415, 1935,
 1963 doi: [10.1111/j.1365-2966.2011.18839.x](https://doi.org/10.1111/j.1365-2966.2011.18839.x)
- 1964 Courtois, H. M., Tully, R. B., Makarov, D. I., et al. 2011b,
 1965 MNRAS, 414, 2005,
 1966 doi: [10.1111/j.1365-2966.2011.18515.x](https://doi.org/10.1111/j.1365-2966.2011.18515.x)
- 1967 Da Costa, G. S., & Armandroff, T. E. 1990, AJ, 100, 162,
 1968 doi: [10.1086/115500](https://doi.org/10.1086/115500)
- 1969 Davis, T. M., & Scrimgeour, M. I. 2014, MNRAS, 442,
 1970 1117, doi: [10.1093/mnras/stu920](https://doi.org/10.1093/mnras/stu920)
- 1971 de Jaeger, T., Stahl, B. E., Zheng, W., et al. 2020a,
 1972 MNRAS, 496, 3402, doi: [10.1093/mnras/staa1801](https://doi.org/10.1093/mnras/staa1801)
- 1973 de Jaeger, T., Galbany, L., González-Gaitán, S., et al.
 1974 2020b, MNRAS, 495, 4860, doi: [10.1093/mnras/staa1402](https://doi.org/10.1093/mnras/staa1402)
- 1975 de Lapparent, V., Geller, M. J., & Huchra, J. P. 1986,
 1976 ApJL, 302, L1, doi: [10.1086/184625](https://doi.org/10.1086/184625)
- 1977 Djorgovski, S., & Davis, M. 1987, ApJ, 313, 59,
 1978 doi: [10.1086/164948](https://doi.org/10.1086/164948)
- 1979 Dressler, A., Faber, S. M., Burstein, D., et al. 1987a, ApJL,
 1980 313, L37, doi: [10.1086/184827](https://doi.org/10.1086/184827)
- 1981 Dressler, A., Lynden-Bell, D., Burstein, D., et al. 1987b,
 1982 ApJ, 313, 42, doi: [10.1086/164947](https://doi.org/10.1086/164947)
- 1983 Dupuy, A., Courtois, H. M., Guinet, D., Tully, R. B., &
 1984 Kourkchi, E. 2021, A&A, 646, A113,
 1985 doi: [10.1051/0004-6361/202039025](https://doi.org/10.1051/0004-6361/202039025)

- 1987 Ferrarese, L., Côté, P., Cuillandre, J.-C., et al. 2012, ApJS,
200, 4, doi: [10.1088/0067-0049/200/1/4](https://doi.org/10.1088/0067-0049/200/1/4)
- 1988 Fixsen, D. J., Cheng, E. S., Gales, J. M., et al. 1996, ApJ,
473, 576, doi: [10.1086/178173](https://doi.org/10.1086/178173)
- 1991 Folatelli, G., Phillips, M. M., Burns, C. R., et al. 2010, AJ,
139, 120, doi: [10.1088/0004-6256/139/1/120](https://doi.org/10.1088/0004-6256/139/1/120)
- 1993 Foreman-Mackey, D., Hogg, D. W., Lang, D., & Goodman,
J. 2013, PASP, 125, 306, doi: [10.1086/670067](https://doi.org/10.1086/670067)
- 1995 Freedman, W. L., Madore, B. F., Gibson, B. K., et al. 2001,
ApJ, 553, 47, doi: [10.1086/320638](https://doi.org/10.1086/320638)
- 1997 Freedman, W. L., Madore, B. F., Hatt, D., et al. 2019, ApJ,
882, 34, doi: [10.3847/1538-4357/ab2f73](https://doi.org/10.3847/1538-4357/ab2f73)
- 1999 Freedman, W. L., Madore, B. F., Hoyt, T., et al. 2020,
ApJ, 891, 57, doi: [10.3847/1538-4357/ab7339](https://doi.org/10.3847/1538-4357/ab7339)
- 2001 Ganeshalingam, M., Li, W., & Filippenko, A. V. 2013,
MNRAS, 433, 2240, doi: [10.1093/mnras/stt893](https://doi.org/10.1093/mnras/stt893)
- 2003 Garofalo, A., Delgado, H. E., Sarro, L. M., et al. 2022,
MNRAS, 513, 788, doi: [10.1093/mnras/stac735](https://doi.org/10.1093/mnras/stac735)
- 2005 Gott, J. Richard, I., Jurić, M., Schlegel, D., et al. 2005,
ApJ, 624, 463, doi: [10.1086/428890](https://doi.org/10.1086/428890)
- 2007 Graziani, R., Courtois, H. M., Lavaux, G., et al. 2019,
MNRAS, 488, 5438, doi: [10.1093/mnras/stz078](https://doi.org/10.1093/mnras/stz078)
- 2009 Hamuy, M., & Pinto, P. A. 2002, ApJL, 566, L63,
doi: [10.1086/339676](https://doi.org/10.1086/339676)
- 2011 Hayden, B. T., Gupta, R. R., Garnavich, P. M., et al. 2013,
ApJ, 764, 191, doi: [10.1088/0004-637X/764/2/191](https://doi.org/10.1088/0004-637X/764/2/191)
- 2013 Haynes, M. P., Giovanelli, R., Martin, A. M., et al. 2011,
AJ, 142, 170, doi: [10.1088/0004-6256/142/5/170](https://doi.org/10.1088/0004-6256/142/5/170)
- 2015 Haynes, M. P., Giovanelli, R., Kent, B. R., et al. 2018, ApJ,
861, 49, doi: [10.3847/1538-4357/aac956](https://doi.org/10.3847/1538-4357/aac956)
- 2017 Hicken, M., Wood-Vasey, W. M., Blondin, S., et al. 2009,
ApJ, 700, 1097, doi: [10.1088/0004-637X/700/2/1097](https://doi.org/10.1088/0004-637X/700/2/1097)
- 2019 Hoffman, Y., Courtois, H. M., & Tully, R. B. 2015,
MNRAS, 449, 4494, doi: [10.1093/mnras/stv615](https://doi.org/10.1093/mnras/stv615)
- 2021 Hoffman, Y., Nusser, A., Valade, A., Libeskind, N. I., &
Tully, R. B. 2021, MNRAS, 505, 3380,
doi: [10.1093/mnras/stab1457](https://doi.org/10.1093/mnras/stab1457)
- 2024 Hong, T., Staveley-Smith, L., Masters, K. L., et al. 2019,
MNRAS, 487, 2061, doi: [10.1093/mnras/stz1413](https://doi.org/10.1093/mnras/stz1413)
- 2026 Howlett, C., Said, K., Lucey, J. R., et al. 2022, MNRAS,
515, 953, doi: [10.1093/mnras/stac1681](https://doi.org/10.1093/mnras/stac1681)
- 2028 Huchra, J. P., Macri, L. M., Masters, K. L., et al. 2012,
ApJS, 199, 26, doi: [10.1088/0067-0049/199/2/26](https://doi.org/10.1088/0067-0049/199/2/26)
- 2030 Hudson, M. J., Lucey, J. R., Smith, R. J., Schlegel, D. J.,
& Davies, R. L. 2001, MNRAS, 327, 265,
doi: [10.1046/j.1365-8711.2001.04786.x](https://doi.org/10.1046/j.1365-8711.2001.04786.x)
- 2033 Humphreys, E. M. L., Reid, M. J., Moran, J. M., Greenhill,
L. J., & Argon, A. L. 2013, ApJ, 775, 13,
doi: [10.1088/0004-637X/775/1/13](https://doi.org/10.1088/0004-637X/775/1/13)
- 2036 Jacobs, B. A., Rizzi, L., Tully, R. B., et al. 2009, AJ, 138,
332, doi: [10.1088/0004-6256/138/2/332](https://doi.org/10.1088/0004-6256/138/2/332)
- 2038 Jang, I. S., & Lee, M. G. 2017, ApJ, 835, 28,
doi: [10.3847/1538-4357/835/1/28](https://doi.org/10.3847/1538-4357/835/1/28)
- 2040 Jarrett, T. H., Chester, T., Cutri, R., et al. 2000, AJ, 119,
2498, doi: [10.1086/301330](https://doi.org/10.1086/301330)
- 2042 Jasche, J., & Lavaux, G. 2019, A&A, 625, A64,
doi: [10.1051/0004-6361/201833710](https://doi.org/10.1051/0004-6361/201833710)
- 2044 Jensen, J. B., Blakeslee, J. P., Gibson, Z., et al. 2015, ApJ,
808, 91, doi: [10.1088/0004-637X/808/1/91](https://doi.org/10.1088/0004-637X/808/1/91)
- 2046 Jensen, J. B., Blakeslee, J. P., Ma, C.-P., et al. 2021, ApJS,
255, 21, doi: [10.3847/1538-4365/ac01e7](https://doi.org/10.3847/1538-4365/ac01e7)
- 2048 Jha, S., Riess, A. G., & Kirshner, R. P. 2007, ApJ, 659,
122, doi: [10.1086/512054](https://doi.org/10.1086/512054)
- 2050 Jones, D. H., Read, M. A., Saunders, W., et al. 2009,
MNRAS, 399, 683, doi: [10.1111/j.1365-2966.2009.15338.x](https://doi.org/10.1111/j.1365-2966.2009.15338.x)
- 2052 Kaiser, N. 1988, MNRAS, 231, 149,
doi: [10.1093/mnras/231.2.149](https://doi.org/10.1093/mnras/231.2.149)
- 2054 Karachentsev, I. D., Makarova, L. N., Tully, R. B., et al.
2017, MNRAS, 469, L113, doi: [10.1093/mnrasl/slx061](https://doi.org/10.1093/mnrasl/slx061)
- 2056 Kourkchi, E., & Tully, R. B. 2017, ApJ, 843, 16,
doi: [10.3847/1538-4357/aa76db](https://doi.org/10.3847/1538-4357/aa76db)
- 2058 Kourkchi, E., Tully, R. B., Anand, G. S., et al. 2020a, ApJ,
896, 3, doi: [10.3847/1538-4357/ab901c](https://doi.org/10.3847/1538-4357/ab901c)
- 2060 Kourkchi, E., Tully, R. B., Courtois, H. M., Dupuy, A., &
Guinet, D. 2022, MNRAS, 511, 6160,
doi: [10.1093/mnras/stac303](https://doi.org/10.1093/mnras/stac303)
- 2063 Kourkchi, E., Tully, R. B., Neill, J. D., et al. 2019, ApJ,
884, 82, doi: [10.3847/1538-4357/ab4192](https://doi.org/10.3847/1538-4357/ab4192)
- 2065 Kourkchi, E., Tully, R. B., Eftekharzadeh, S., et al. 2020b,
ApJ, 902, 145, doi: [10.3847/1538-4357/abb66b](https://doi.org/10.3847/1538-4357/abb66b)
- 2067 Leavitt, H. S., & Pickering, E. C. 1912, Harvard College
Observatory Circular, 173, 1
- 2069 Lee, M. G., Freedman, W. L., & Madore, B. F. 1993, ApJ,
417, 553, doi: [10.1086/173334](https://doi.org/10.1086/173334)
- 2071 Lelli, F., McGaugh, S. S., & Schombert, J. M. 2016, ApJL,
816, L14, doi: [10.3847/2041-8205/816/1/L14](https://doi.org/10.3847/2041-8205/816/1/L14)
- 2073 Lelli, F., McGaugh, S. S., Schombert, J. M., Desmond, H.,
& Katz, H. 2019, MNRAS, 484, 3267,
doi: [10.1093/mnras/stz205](https://doi.org/10.1093/mnras/stz205)
- 2076 Lilow, R., & Nusser, A. 2021, MNRAS, 507, 1557,
doi: [10.1093/mnras/stab2009](https://doi.org/10.1093/mnras/stab2009)
- 2078 Lim, S. H., Mo, H. J., Lu, Y., Wang, H., & Yang, X. 2017,
MNRAS, 470, 2982, doi: [10.1093/mnras/stx1462](https://doi.org/10.1093/mnras/stx1462)
- 2080 Ma, C.-P., Greene, J. E., McConnell, N., et al. 2014, ApJ,
795, 158, doi: [10.1088/0004-637X/795/2/158](https://doi.org/10.1088/0004-637X/795/2/158)
- 2082 Madore, B. F., & Freedman, W. L. 1995, AJ, 109, 1645,
doi: [10.1086/117391](https://doi.org/10.1086/117391)
- 2084 Magoulas, C., Springob, C. M., Colless, M., et al. 2012,
MNRAS, 427, 245, doi: [10.1111/j.1365-2966.2012.21421.x](https://doi.org/10.1111/j.1365-2966.2012.21421.x)

- 2086 Mainzer, A., Bauer, J., Grav, T., et al. 2011, ApJ, 731, 53,
2087 doi: [10.1088/0004-637X/731/1/53](https://doi.org/10.1088/0004-637X/731/1/53)
- 2088 Makarov, D., Makarova, L., Rizzi, L., et al. 2006, AJ, 132,
2089 2729, doi: [10.1086/508925](https://doi.org/10.1086/508925)
- 2090 Makarov, D. I., Zaitseva, N. A., & Bizyaev, D. V. 2018,
2091 MNRAS, 479, 3373, doi: [10.1093/mnras/sty1629](https://doi.org/10.1093/mnras/sty1629)
- 2092 Makarova, L. N., Makarov, D. I., Karachentsev, I. D.,
2093 Tully, R. B., & Rizzi, L. 2017, MNRAS, 464, 2281,
2094 doi: [10.1093/mnras/stw2502](https://doi.org/10.1093/mnras/stw2502)
- 2095 Maoz, D., Mannucci, F., & Nelemans, G. 2014, ARA&A,
2096 52, 107, doi: [10.1146/annurev-astro-082812-141031](https://doi.org/10.1146/annurev-astro-082812-141031)
- 2097 McGaugh, S. S. 2005, ApJ, 632, 859, doi: [10.1086/432968](https://doi.org/10.1086/432968)
- 2098 McGaugh, S. S., Schombert, J. M., Bothun, G. D., & de
2099 Blok, W. J. G. 2000, ApJL, 533, L99, doi: [10.1086/312628](https://doi.org/10.1086/312628)
- 2100 McQuinn, K. B. W., Skillman, E. D., Dolphin, A. E., Berg,
2101 D., & Kennicutt, R. 2017, AJ, 154, 51,
2102 doi: [10.3847/1538-3881/aa7aad](https://doi.org/10.3847/1538-3881/aa7aad)
- 2103 Mei, S., Blakeslee, J. P., Côté, P., et al. 2007, ApJ, 655,
2104 144, doi: [10.1086/509598](https://doi.org/10.1086/509598)
- 2105 Méndez, B., Davis, M., Moustakas, J., et al. 2002, AJ, 124,
2106 213, doi: [10.1086/341168](https://doi.org/10.1086/341168)
- 2107 Monelli, M., Fiorentino, G., Bernard, E. J., et al. 2017,
2108 ApJ, 842, 60, doi: [10.3847/1538-4357/aa738d](https://doi.org/10.3847/1538-4357/aa738d)
- 2109 Mould, J., Clementini, G., & Da Costa, G. 2019, PASA, 36,
2110 e001, doi: [10.1017/pasa.2018.46](https://doi.org/10.1017/pasa.2018.46)
- 2111 Nagarajan, P., Weisz, D. R., & El-Badry, K. 2022, ApJ,
2112 932, 19, doi: [10.3847/1538-4357/ac69e6](https://doi.org/10.3847/1538-4357/ac69e6)
- 2113 Paturel, G., Garnier, R., Petit, C., & Marthinet, M. C.
2114 1996, A&A, 311, 12
- 2115 Pesce, D. W., Braatz, J. A., Reid, M. J., et al. 2020, ApJL,
2116 891, L1, doi: [10.3847/2041-8213/ab75f0](https://doi.org/10.3847/2041-8213/ab75f0)
- 2117 Phillips, M. M. 1993, ApJL, 413, L105, doi: [10.1086/186970](https://doi.org/10.1086/186970)
- 2118 Pietrzyński, G., Graczyk, D., Gallenne, A., et al. 2019,
2119 Nature, 567, 200, doi: [10.1038/s41586-019-0999-4](https://doi.org/10.1038/s41586-019-0999-4)
- 2120 Prieto, J. L., Rest, A., & Suntzeff, N. B. 2006, ApJ, 647,
2121 501, doi: [10.1086/504307](https://doi.org/10.1086/504307)
- 2122 Qin, F., Howlett, C., & Staveley-Smith, L. 2019, MNRAS,
2123 487, 5235, doi: [10.1093/mnras/stz1576](https://doi.org/10.1093/mnras/stz1576)
- 2124 Qin, F., Howlett, C., Staveley-Smith, L., & Hong, T. 2018,
2125 MNRAS, 477, 5150, doi: [10.1093/mnras/sty928](https://doi.org/10.1093/mnras/sty928)
- 2126 Reid, M. J., Pesce, D. W., & Riess, A. G. 2019, ApJL, 886,
2127 L27, doi: [10.3847/2041-8213/ab552d](https://doi.org/10.3847/2041-8213/ab552d)
- 2128 Rest, A., Scolnic, D., Foley, R. J., et al. 2014, ApJ, 795, 44,
2129 doi: [10.1088/0004-637X/795/1/44](https://doi.org/10.1088/0004-637X/795/1/44)
- 2130 Riess, A. G., Casertano, S., Yuan, W., et al. 2021, ApJL,
2131 908, L6, doi: [10.3847/2041-8213/abdbaf](https://doi.org/10.3847/2041-8213/abdbaf)
- 2132 Riess, A. G., Casertano, S., Yuan, W., Macri, L. M., &
2133 Scolnic, D. 2019, ApJ, 876, 85,
2134 doi: [10.3847/1538-4357/ab1422](https://doi.org/10.3847/1538-4357/ab1422)
- 2135 Riess, A. G., Macri, L. M., Hoffmann, S. L., et al. 2016,
2136 ApJ, 826, 56, doi: [10.3847/0004-637X/826/1/56](https://doi.org/10.3847/0004-637X/826/1/56)
- 2137 Riess, A. G., Casertano, S., Yuan, W., et al. 2018, ApJ,
2138 861, 126, doi: [10.3847/1538-4357/aac82e](https://doi.org/10.3847/1538-4357/aac82e)
- 2139 Riess, A. G., Yuan, W., Macri, L. M., et al. 2022, ApJL,
2140 934, L7, doi: [10.3847/2041-8213/ac5c5b](https://doi.org/10.3847/2041-8213/ac5c5b)
- 2141 Rizzi, L., Tully, R. B., Makarov, D., et al. 2007, ApJ, 661,
2142 815, doi: [10.1086/516566](https://doi.org/10.1086/516566)
- 2143 Roman, M., Hardin, D., Betoule, M., et al. 2018, A&A,
2144 615, A68, doi: [10.1051/0004-6361/201731425](https://doi.org/10.1051/0004-6361/201731425)
- 2145 Salaris, M., & Cassisi, S. 2005, Evolution of Stars and
2146 Stellar Populations
- 2147 Scolnic, D., Brout, D., Carr, A., et al. 2021, arXiv e-prints,
2148 arXiv:2112.03863. <https://arxiv.org/abs/2112.03863>
- 2149 Serenelli, A., Weiss, A., Cassisi, S., Salaris, M., &
2150 Pietrinferni, A. 2017, A&A, 606, A33,
2151 doi: [10.1051/0004-6361/201731004](https://doi.org/10.1051/0004-6361/201731004)
- 2152 Shaya, E. J., Tully, R. B., Hoffman, Y., & Pomarède, D.
2153 2017, ApJ, 850, 207, doi: [10.3847/1538-4357/aa9525](https://doi.org/10.3847/1538-4357/aa9525)
- 2154 Skrutskie, M. F., Cutri, R. M., Stiening, R., et al. 2006, AJ,
2155 131, 1163, doi: [10.1086/498708](https://doi.org/10.1086/498708)
- 2156 Soltis, J., Casertano, S., & Riess, A. G. 2021, ApJL, 908,
2157 L5, doi: [10.3847/2041-8213/abdbad](https://doi.org/10.3847/2041-8213/abdbad)
- 2158 Sorce, J. G., Courtois, H. M., & Tully, R. B. 2012, AJ, 144,
2159 133, doi: [10.1088/0004-6256/144/5/133](https://doi.org/10.1088/0004-6256/144/5/133)
- 2160 Sorce, J. G., Tully, R. B., Courtois, H. M., et al. 2014,
2161 MNRAS, 444, 527, doi: [10.1093/mnras/stu1450](https://doi.org/10.1093/mnras/stu1450)
- 2162 Springob, C. M., Masters, K. L., Haynes, M. P., Giovanelli,
2163 R., & Marinoni, C. 2007, ApJS, 172, 599,
2164 doi: [10.1086/519527](https://doi.org/10.1086/519527)
- 2165 Springob, C. M., Magoulas, C., Colless, M., et al. 2014,
2166 MNRAS, 445, 2677, doi: [10.1093/mnras/stu1743](https://doi.org/10.1093/mnras/stu1743)
- 2167 Stahl, B. E., de Jaeger, T., Boruah, S. S., et al. 2021,
2168 MNRAS, doi: [10.1093/mnras/stab1446](https://doi.org/10.1093/mnras/stab1446)
- 2169 Tempel, E., Saar, E., Liivamägi, L. J., et al. 2011, A&A,
2170 529, A53, doi: [10.1051/0004-6361/201016196](https://doi.org/10.1051/0004-6361/201016196)
- 2171 Tempel, E., Tuvikene, T., Kipper, R., & Libeskind, N. I.
2172 2017, A&A, 602, A100,
2173 doi: [10.1051/0004-6361/201730499](https://doi.org/10.1051/0004-6361/201730499)
- 2174 Tempel, E., Tamm, A., Gramann, M., et al. 2014, A&A,
2175 566, A1, doi: [10.1051/0004-6361/201423585](https://doi.org/10.1051/0004-6361/201423585)
- 2176 Thomas, D., Steele, O., Maraston, C., et al. 2013, MNRAS,
2177 431, 1383, doi: [10.1093/mnras/stt261](https://doi.org/10.1093/mnras/stt261)
- 2178 Tonry, J., & Schneider, D. P. 1988, AJ, 96, 807,
2179 doi: [10.1086/114847](https://doi.org/10.1086/114847)
- 2180 Tonry, J. L., Dressler, A., Blakeslee, J. P., et al. 2001, ApJ,
2181 546, 681, doi: [10.1086/318301](https://doi.org/10.1086/318301)
- 2182 Tully, R. B. 2015a, AJ, 149, 54,
2183 doi: [10.1088/0004-6256/149/2/54](https://doi.org/10.1088/0004-6256/149/2/54)
- 2184 —. 2015b, AJ, 149, 171, doi: [10.1088/0004-6256/149/5/171](https://doi.org/10.1088/0004-6256/149/5/171)

- 2185 Tully, R. B., Courtois, H. M., & Sorce, J. G. 2016, AJ, 152, 50, doi: [10.3847/0004-6256/152/2/50](https://doi.org/10.3847/0004-6256/152/2/50)
- 2186 Tully, R. B., & Fisher, J. R. 1977, A&A, 54, 661
- 2187 Tully, R. B., Shaya, E. J., Karachentsev, I. D., et al. 2008, ApJ, 676, 184, doi: [10.1086/527428](https://doi.org/10.1086/527428)
- 2188 Tully, R. B., Courtois, H. M., Dolphin, A. E., et al. 2013, AJ, 146, 86, doi: [10.1088/0004-6256/146/4/86](https://doi.org/10.1088/0004-6256/146/4/86)
- 2189 Vogeley, M. S., Hoyle, F., Rojas, R. R., & Goldberg, D. M. 2004, in IAU Colloq. 195: Outskirts of Galaxy Clusters: Intense Life in the Suburbs, ed. A. Diaferio, 5–11, doi: [10.1017/S1743921304000043](https://doi.org/10.1017/S1743921304000043)
- 2190 Walker, E. S., Baltay, C., Campillay, A., et al. 2015, ApJS, 219, 13, doi: [10.1088/0067-0049/219/1/13](https://doi.org/10.1088/0067-0049/219/1/13)
- 2191 Watkins, R., & Feldman, H. A. 2015, MNRAS, 450, 1868, doi: [10.1093/mnras/stv651](https://doi.org/10.1093/mnras/stv651)
- 2192 Wright, E. L., Eisenhardt, P. R. M., Mainzer, A. K., et al. 2010, AJ, 140, 1868, doi: [10.1088/0004-6256/140/6/1868](https://doi.org/10.1088/0004-6256/140/6/1868)
- 2193 Wu, P.-F., Tully, R. B., Rizzi, L., et al. 2014, AJ, 148, 7, doi: [10.1088/0004-6256/148/1/7](https://doi.org/10.1088/0004-6256/148/1/7)
- 2194 York, D. G., Adelman, J., Anderson, John E., J., et al. 2000, AJ, 120, 1579, doi: [10.1086/301513](https://doi.org/10.1086/301513)
- 2195 Yuan, W., Riess, A. G., Macri, L. M., Casertano, S., & Scolnic, D. M. 2019, ApJ, 886, 61, doi: [10.3847/1538-4357/ab4bc9](https://doi.org/10.3847/1538-4357/ab4bc9)
- 2196 Yuan, W., Fausnaugh, M. M., Hoffmann, S. L., et al. 2020, ApJ, 902, 26, doi: [10.3847/1538-4357/abb377](https://doi.org/10.3847/1538-4357/abb377)
- 2197 Yuan, W., Macri, L. M., Peterson, B. M., et al. 2021, ApJ, 913, 3, doi: [10.3847/1538-4357/abf24a](https://doi.org/10.3847/1538-4357/abf24a)
- 2198 Zgirski, B., Gieren, W., Pietrzyński, G., et al. 2017, ApJ, 847, 88, doi: [10.3847/1538-4357/aa88c4](https://doi.org/10.3847/1538-4357/aa88c4)
- 2199